

**High Precision Tracking Control Applied to Spiral Servo Writing
in Hard Disk Drives**

by

Xu Chen

B.S. (Tsinghua University) 2008

A dissertation submitted in partial satisfaction of the
requirements for the degree of
Master of Science

in

Engineering - Mechanical Engineering

in the

GRADUATE DIVISION

of the

UNIVERSITY OF CALIFORNIA, BERKELEY

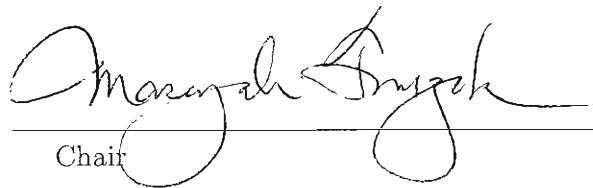
Committee in charge:

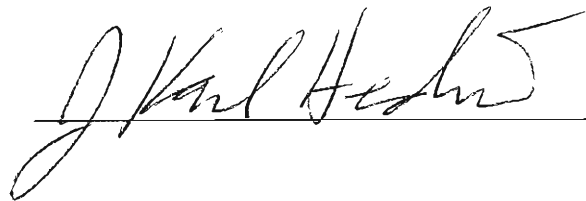
Professor Masayoshi Tomizuka, Chair

Professor J. Karl Hedrick

Spring 2010

The dissertation of Xu Chen is approved:

 5/4/10
Chair Date

 5/14/10
Date

Date

University of California, Berkeley

Spring 2010

**High Precision Tracking Control Applied to Spiral Servo Writing
in Hard Disk Drives**

Copyright 2010

by

Xu Chen

Abstract

High Precision Tracking Control Applied to Spiral Servo Writing
in Hard Disk Drives

by

Xu Chen

Master of Science in Engineering - Mechanical Engineering

University of California, Berkeley

Professor Masayoshi Tomizuka, Chair

As the tracks-per-inch (TPI) gets higher and higher in hard disk drives (HDDs), servo writing takes a longer and longer time. One way to solve this problem is to use servo track writers to write spiral servo patterns on the disks and then perform self servo writing (SSW) within each HDD unit. The quality of the spirals is the key to achieve high TPI in SSW. This report discusses high precision tracking control algorithms for the writing of spiral servo patterns. The Zero Phase Error Tracking (ZPET) technique and a new disturbance observer (DOB) design algorithm are first introduced in writing one stroke of spiral. Extending this controller structure to multiple spiral writing, an Iterative Learning Control (ILC) algorithm is then introduced, which retains the advantages of the ZPET plus modified DOB structure, and generates an asymptotically optimal feedforward input. Non-repetitive disturbances going into the learning system have an adverse influence on the tracking performance. The report analyzes this situation, develops and presents three effective methods to deal with the problem.



Professor Masayoshi Tomizuka
Dissertation Committee Chair

Contents

List of Figures	iii
1 Introduction	1
1.1 Data Arrangement and Access in Hard Disk Drives	1
1.2 Hardware Description	5
1.3 Control Issues in Spiral Writing	7
1.4 Organization of the Report	8
2 System Identification	9
2.1 FEA Model and Frequency Response of the Servo System	9
2.2 System Model Used in Simulation	14
3 Robust High Precision Tracking Control for Single Spiral Writing	16
3.1 Trajectory Design	16
3.2 Overall Controller Structure	18
3.3 Disturbance Observer Design	19
3.3.1 Review of Standard DOB	19
3.3.1.1 Standard Structure	19
3.3.1.2 Stability Robustness	23
3.3.2 DOB Based on Optimal Plant Shaping	25
3.3.2.1 Controller Structure and Properties	25
3.3.2.2 Stability Robustness	26
3.3.2.3 Shaping Filter Design	27
3.3.2.4 Optimal Plant Shaping From the View Point of Nom- inal Model	31
3.4 Zero Phase Error Tracking for Improved Spiral Writing	32
3.5 Simulation Results	35
3.5.1 Deterministic Tracking	35
3.5.2 Tracking in the Presence of External Disturbances	37
3.6 Summary	41

4	Iterative Learning Control for Multiple Spiral Writing	43
4.1	Trajectory Design	46
4.2	Iterative Learning Control Design	47
	4.2.1 Control Law Derivation	47
	4.2.2 Stability and Robust Stability	49
4.3	Simulation Results	51
	4.3.1 Deterministic Tracking	52
	4.3.2 Tracking in the Presence of External Disturbances	53
4.4	Summary	55
5	Robust Iterative Learning Control	56
5.1	Multi-iteration ILC	56
5.2	ILC Based on Adaptive Repetitive Error Estimation	58
5.3	ILC Based on Repeatable Disturbance Estimation	60
5.4	Summary	63
6	Conclusions and Future Research	65
	Bibliography	67
A	Proof of Theorem 4.1	69

List of Figures

1.1	Data tracks and servo sectors on hard disks.	2
1.2	The two types of servo patterns on the disk. Left figure: spiral servo patterns written on a blank disk; Right figure: drive servo patterns written based on the spiral servo patterns.	2
1.3	The three velocity regions for the head to move from OD to ID.	3
1.4	Multiple spiral writing on a disk surface.	4
1.5	A possible spiral writing trajectory profile.	4
1.6	Sync marks in spirals.	5
1.7	A stack of disks mounted on a hub.	5
1.8	A group of actuator arms controlled by VCM.	6
1.9	Disk assembly with actuator arms and air shroud.	6
2.1	FEA model of the servo track writer.	10
2.2	Frequency response of the head system.	10
2.3	Plant vibration mode: base bending at 1567 Hz.	11
2.4	Plant vibration mode: base bending at 1781 Hz.	12
2.5	Plant vibration mode: base torsion (butterfly) at 4802 Hz.	12
2.6	Plant vibration mode: suspension 2nd bending at 8844 Hz.	13
2.7	Plant vibration mode: suspension sway at 13128 Hz.	13
2.8	Frequency response of the dynamic model used in simulation.	15
3.1	The three regions for the head to move from OD to ID.	17
3.2	Desired trajectory profile for moving the head from OD to ID.	18
3.3	Proposed controller structure for single spiral writing.	19
3.4	Block diagram of the standard digital DOB.	21
3.5	Equivalent form 1 of the standard DOB.	21
3.6	Equivalent form 2 of the standard DOB.	22
3.7	Frequency response of a Q-filter with a cut-off frequency of 2000 Hz.	23
3.8	Magnitude responses of $Q(z^{-1})$ and $1/\Delta(z^{-1})$ in the standard DOB: cut-off frequency of Q-filter restricted to be below 320 Hz.	24
3.9	Block diagram: DOB based on optimal plant shaping.	25

3.10	Frequency responses of the plant, the nominal plant, the optimally shaped plant, and the plant with initial shaping filter guess.	29
3.11	Frequency response of the optimal shaping filter.	30
3.12	Magnitude responses of $Q(z^{-1})$ and $1/\Delta(z^{-1})$ in the proposed DOB: Q-filter cut-off frequency can expand to as large as 2000 Hz.	30
3.13	Equivalent form one of the proposed DOB.	31
3.14	Equivalent form two of the proposed DOB.	31
3.15	Equivalent loop transformation of the proposed DOB.	32
3.16	Overall controller structure applying the DOB based on optimal plant shaping.	33
3.17	Practical implementation of the ZPET control algorithm.	34
3.18	Magnitude responses of $G_{overall}(z^{-1})$ with and without E-filter (sampling frequency: 26400 Hz).	35
3.19	Simulated position tracking result.	36
3.20	Simulated position tracking error.	37
3.21	Block diagram of the proposed control structure in noisy environments	38
3.22	The repeatable output disturbance data.	38
3.23	Spectrum of the non-repeatable disturbance.	39
3.24	Simulated position tracking result in a noisy environment.	39
3.25	Spectrum of the simulated position tracking error in a noisy environment.	40
3.26	Time traces of the tracking errors.	41
3.27	Frequency spectra of the tracking error.	41
3.28	Magnitude response from input disturbance to plant output.	42
4.1	Block diagram of ILC combined with ZPET control: the first trial . .	45
4.2	Block diagram of ILC combined with ZPET control: 2^{nd} trial.	45
4.3	Block diagram of ILC combined with ZPET control: j^{th} trial ($j > 1$)	45
4.4	Equivalent form of the proposed ILC algorithm.	46
4.5	Reference trajectory for one trial.	47
4.6	Equivalent block diagram of ILC combined with ZPET control	48
4.7	Pole zero map of a zero phase low-pass filter.	51
4.8	Simulated frequency response of a low-pass filter.	51
4.9	Simulated tracking errors in the deterministic reference tracking: each trial lasts one second, the time traces of all the 14 trials are stacked into a long vector to demonstrate the tracking performance.	52
4.10	Norms of the simulated tracking errors in the deterministic reference tracking.	53
4.11	Comparison of the simulated error spectra: first and 30^{th} iteration. . .	54
4.12	l_∞ norms of the simulated tracking errors with external disturbance. .	54
4.13	Simulated tracking errors with enhanced repetitive disturbance. . . .	55

5.1	Norms of the simulated errors: ILC control law updated 7 times in 56 repetitions.	57
5.2	Simulated tracking errors when no external repetitive disturbance is present.	58
5.3	Block diagram of ILC based on adaptive repetitive error estimation .	59
5.4	Norms of simulated errors: ILC based on adaptive minimum mean square repetitive error estimation.	60
5.5	Block diagram of the ILC based repetitive disturbance compensation algorithm.	61
5.6	Norms of simulated errors: ILC based on non-repetitive disturbance estimation.	63
5.7	Repetitive disturbance rejection performance.	63

Chapter 1

Introduction

1.1 Data Arrangement and Access in Hard Disk Drives

In modern hard disk drives, writing of data/information is achieved by alternating the polarity of current in the write head's coil. During data writing, the disk spins and the write head is positioned at the desired disk location with as low variance as possible. As a result, data is stored in circular patterns of magnetization known as data tracks or simply, tracks.

For the read/write head to access the disk data, information of the track number and data location within the track should be accessible. Servo sectors are specially coded magnetic patterns written on the disks that provide the location information for the heads. Figure 1.1 is a demonstration of the data tracks and servo sectors on a disk. A typical disk platter in the year of 2007 has more than 100,000 tracks within one inch and more than 220 sectors on one track [1]. As the TPI gets higher and higher, writing of the servo patterns takes a longer and longer time. This requires additional investment on servo track writers which translate to an increased production cost. Spirals servo writing is therefore introduced to reduce the servo writing cost.

As shown in Fig. 1.2, two types of servo patterns exist in the spiral based servo writing process: the spiral servo patterns for manufacturing purpose and the concentric servo patterns, a.k.a. drive servo patterns, for track seeking and following in the daily operation of a HDD unit. These two patterns are written in a two-step manner.

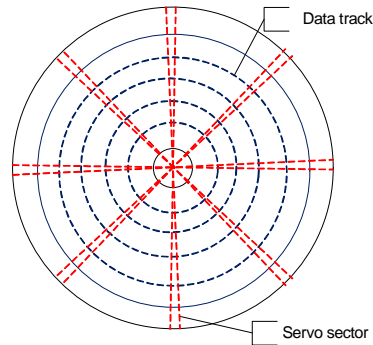


Figure 1.1: Data tracks and servo sectors on hard disks.

In step one, spiral servo patterns are written on an external servo writer. In step two, using the spirals as references, the final product servo patterns are written via in-drive self servo writing.

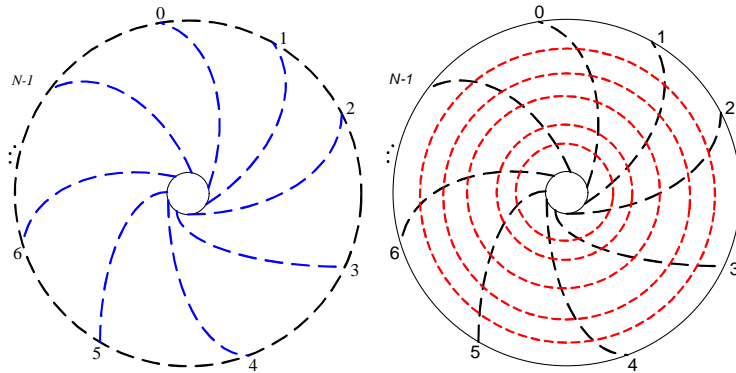


Figure 1.2: The two types of servo patterns on the disk. Left figure: spiral servo patterns written on a blank disk; Right figure: drive servo patterns written based on the spiral servo patterns.

When writing a spiral, the external servo writer controls the radial location of the head for writing a plurality of spiral reference patterns between an inner circular seed track and an outer circular seed track. In an ideal writing process from the outer diameter (OD) to the inner diameter (ID), the head should follow a pre-designed

velocity profile, which typically includes three regions as shown in Fig. 1.3: an acceleration region for the head to reach the desired spiral writing speed, a constant speed spiral writing region, and a deceleration region to reach zero speed when approaching the ID. The acceleration and deceleration distances should be kept as small as possible. Typical spiral writing speed is between two to six inches per second, and the disk rotates fully about 10 times for each spiral.

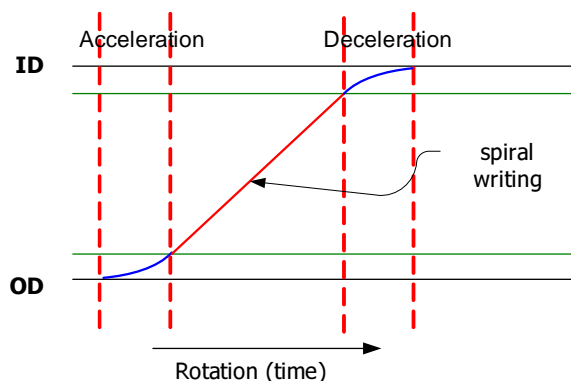


Figure 1.3: The three velocity regions for the head to move from OD to ID.

When writing multiple spirals on a disk, the servo writer head moves back and forth between OD and ID. Figure 1.4 demonstrates an example of writing 8 spirals on a disk. Figure 1.5 is a possible trajectory for a complete moving cycle from OD to ID and then back to OD. As shown in Fig. 1.4, the seed track at the outer diameter contains timing information for spiral writing. The interrupts O1, O2, \dots , and O8 indicate the starting positions for the 8 spirals. When writing the first spiral, the head initializes at position O1 and finishes writing at the seed track in ID. After a short settling at ID, the head “re-traces” to return to the seed track at OD, and waits for the writing position of the next spiral. Preferably, returning to OD should be performed as fast as possible based on the available maximum energy and system component characteristics. Notice that when coming back from ID to OD, the head can not write spirals due to the inverse of the velocity direction. Also worth noticing is that a sequential manner of writing multiple spirals is not necessary, i.e, writing of the second spiral does not need to start at O2. Instead, the spirals can be written in

a more complex or even random manner, as long as the software keeps tracking the starting positions of spirals that have been written¹.

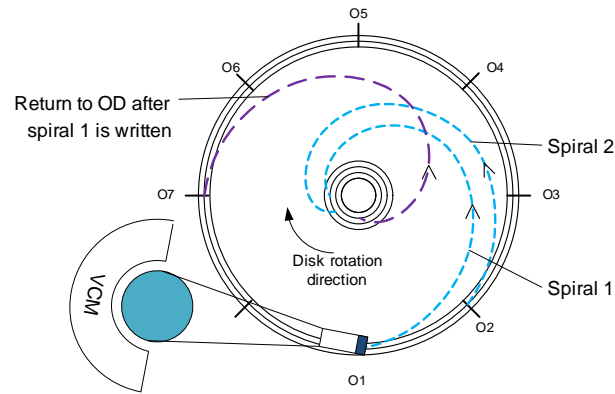


Figure 1.4: Multiple spiral writing on a disk surface.

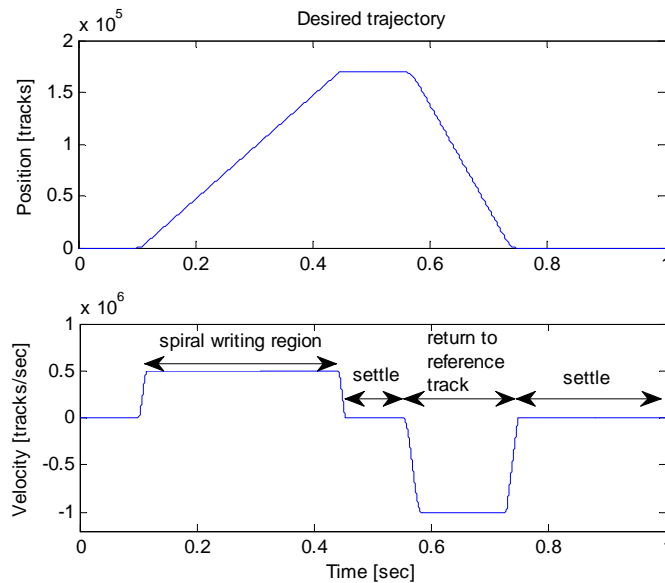


Figure 1.5: A possible spiral writing trajectory profile.

At fixed intervals, a sync pattern/mark is embedded to the spirals. For the servo information to properly perform its function, the same amount of sync marks should

¹In fact, it is beneficial to use a complex spiral sequence due to the thermal expansion of the disk.

lie on each spiral. If we index the sync marks from 1 to N between OD and ID, then sync marks with the same index number i ($1 \leq i \leq N$) should lie on the same radius and be circumferentially equally spaced, as shown in Fig. 1.6.

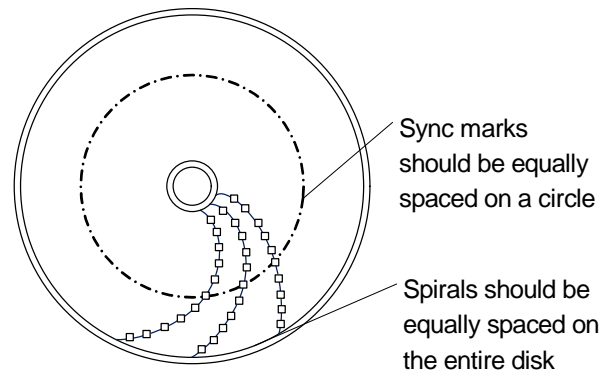


Figure 1.6: Sync marks in spirals.

1.2 Hardware Description

The spiral servo writing process is performed on a media servo writer [2] in a clean room. Several disks are stacked and packed in a disk hub which is attached to a rotating shaft, as shown in Fig. 1.7. The servo writer heads are fixed on another stack of actuator arms controlled by a voice coil motor (VCM), as shown in Fig. 1.8. By servo-writing multiple disks at the same time, the usage of clean room space and the consumption of time can be substantially reduced.

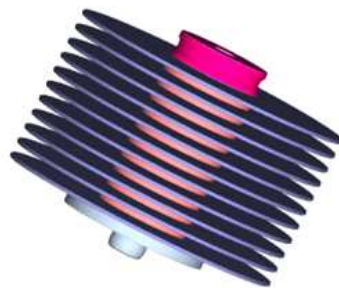


Figure 1.7: A stack of disks mounted on a hub.

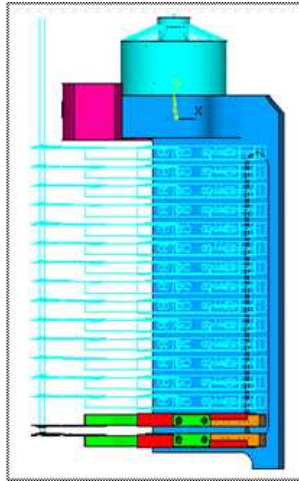


Figure 1.8: A group of actuator arms controlled by VCM.

During the writing process, disks keep spinning at a typical speed of 5400 rpm or 7200 rpm. A flexible air baffle device is applied to reduce the vibration caused by any possible air disturbance. Figure 1.9 gives a graphical demonstration of the assembled disks with air baffle protection.

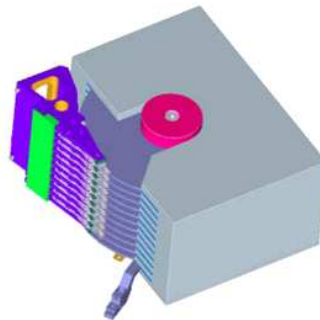


Figure 1.9: Disk assembly with actuator arms and air shroud.

Table 1.1 is a quick summary for the media servo writer machine. Data is collected mainly from the product introduction of LaserResearch Pte Ltd website [2].

Table 1.1: Summary of the media servo writer machine.

Number of Platters	10 disks
Spindle Speed	5400rpm (2400~10000 flexible)
Spindle / Hub	
Jitter	< 0.01%
Spindle NRRO	0.14 micro-inch
Total RRO	0.60 micro-inch
Rotary Positioner and Clock Head	
Encoder Resolution	0.01 micro-inch
Track Holding Accuracy	< 0.12 micro-inch
Settling Time	2.0 ms
Clock Writing Resolution	< 0.001 ns at 10 MHZ
Electronics/System	
Maximum Frequency	300 MHz
Clock Closure	< 2 ns
Phase-lock Loop Jitter	< 100 ps/1 ns
Track to Track Phase	< 0.5 ns/5 ns
Facility Requirement	
Machine Footprint	660 mm×410 mm×1200 mm
Cleanliness	Class 10
Power Supply	110 VAC at 60 Hz, 7 A single phase

1.3 Control Issues in Spiral Writing

The media servo writer comprises head positioning mechanics to derive the radial location of the head. Precise positioning and timing are required when servo patterns are laid down on the disk surface. The radial and circumferential positions of the head need to be well controlled, this results in a position tracking problem. The timing for the sync marks should also be as accurate as possible with additional robustness to

the possible thermal effects of the disk and spindle.

This report focuses on the position control problem in spiral writing. The control objectives are:

- Improve bandwidth of the position control loop system as high as possible;
- Minimize the acceleration region and ensure smooth settling when entering the constant speed spiral writing region;
- Reduce the influences of disturbance (disk modes, windage, friction, thermal expansion, etc);

1.4 Organization of the Report

In Chapter 2, system identification of the servo writer is provided. It will be shown that the dynamic behavior of the servo writer is quite similar to that of an actuator in modern hard disk drives. In Chapter 3, zero phase error tracking (ZPET) control and a modified disturbance observer (DOB) are applied to the position control of writing one stroke of spiral servo patterns. In Chapter 4, the repetitive writing of multiple spirals is analyzed. A novel control algorithm that combines iterative learning control (ILC) with ZPET and DOB is introduced and tested in simulation. Chapter 5 discusses methods to reduce the non-repetitive error influence in ILC. Chapter 6 concludes the report.

Chapter 2

System Identification

2.1 FEA Model and Frequency Response of the Servo System

Figure 2.1 shows the finite element analysis (FEA) model of the servo writer system. For simplicity, the head and actuator pair at the bottom of Fig. 2.1 is called the lower head system, and the one above it named the upper head system. Figure 2.2 shows the frequency responses of the lower and the upper head systems (input: amplitude; output: deg). It is noted that the two systems only have small variances in the frequency region higher than 10,000 Hz. For analysis purpose, the dynamic model of either of them can be applied as the system model in the proposed single input single output (SISO) control.

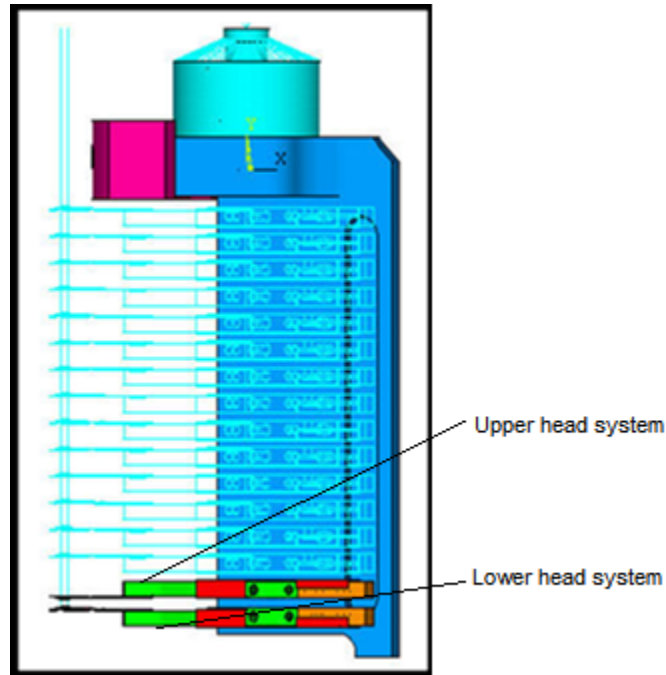


Figure 2.1: FEA model of the servo track writer.

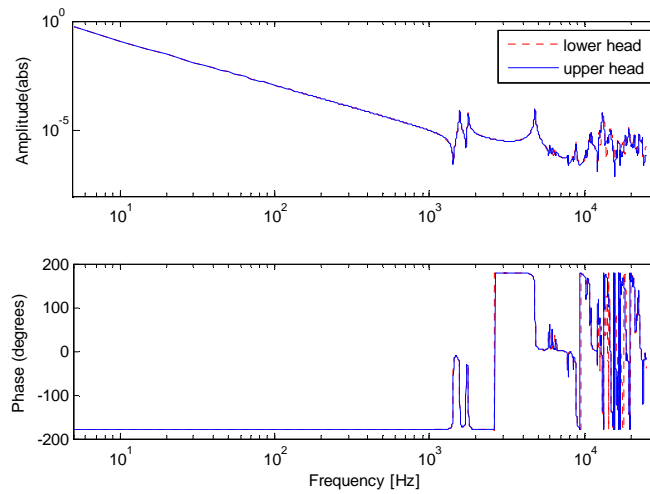


Figure 2.2: Frequency response of the head system.

In the low frequency dynamics, if we consider the servo writer head and actuator system as a rigid body, and the VCM as an ideal transformer [1], a working model of

the VCM actuator plus the driver can be derived as a double integrator

$$G_n(s) = \frac{K_0}{s^2}. \quad (2.1)$$

This also suits well with the FEA frequency response result, which has a -40 dB/dec slope in the low frequency region.

In the high frequency region, similar to modern disk drives, resonance/vibration modes are the major sources of non-repeatable run outs (NRROs) in servo writers. Observing from the FEA results, we find several important vibration modes at respectively 1567 Hz, 1781 Hz, 4802 Hz, 8844 Hz, and 13128 Hz, as shown in Figs. 2.3, 2.4, 2.5, 2.6, and 2.7. They correspond to the base bending and torsion (butterfly) modes, and the suspension bending and sway modes. The dominating vibration modes are approximated by second order under-damped systems. The system dynamic model is finally derived as a summation of the double integrator model plus the dominating vibration modes. Table 2.1 summarizes the identified parameters using the *System Identification Tool Box* in MATLAB.

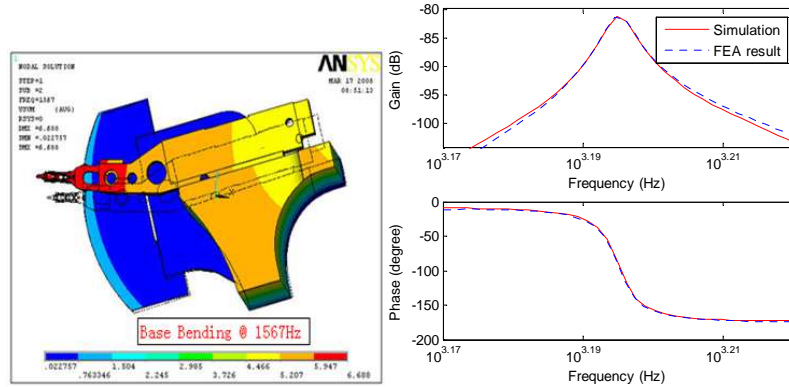


Figure 2.3: Plant vibration mode: base bending at 1567 Hz.

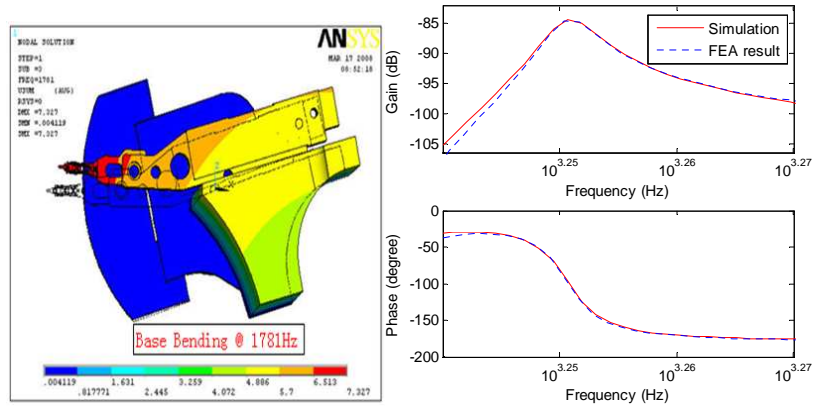


Figure 2.4: Plant vibration mode: base bending at 1781 Hz.

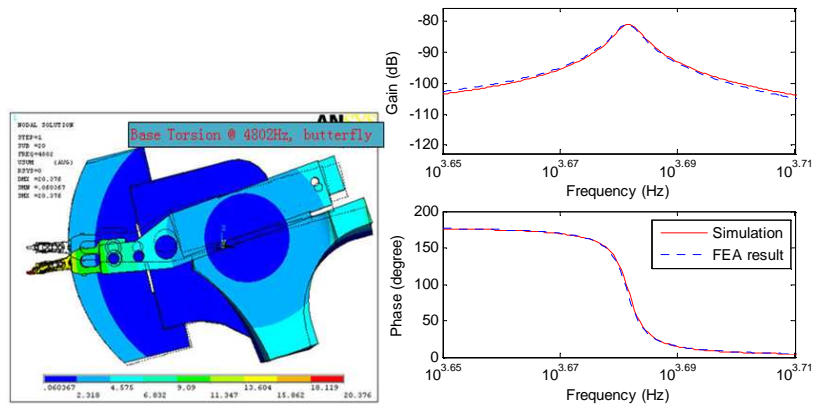


Figure 2.5: Plant vibration mode: base torsion (butterfly) at 4802 Hz.

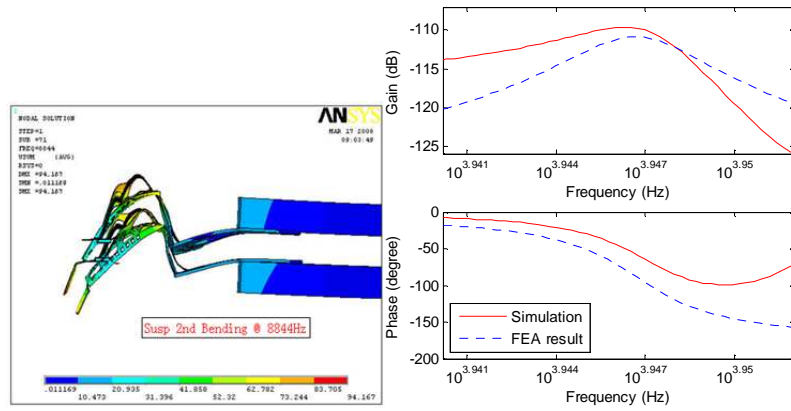


Figure 2.6: Plant vibration mode: suspension 2nd bending at 8844 Hz.

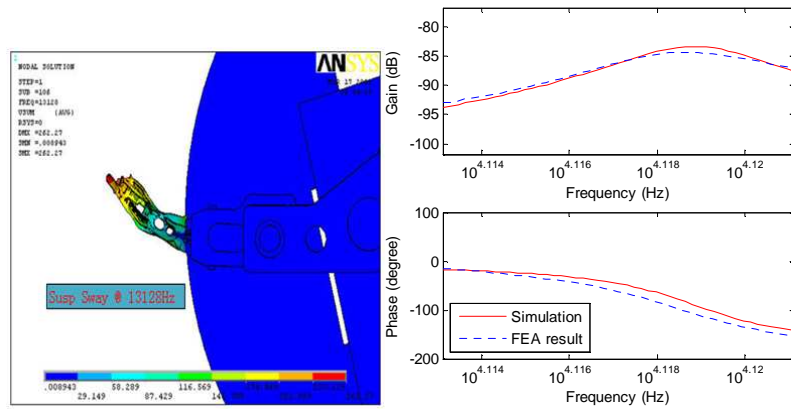


Figure 2.7: Plant vibration mode: suspension sway at 13128 Hz.

Table 2.1: Model parameters

	Low frequency	High frequency				
		Base 1 st bend	Base 2 nd bend	Base Torsion	Suspension 2 nd bend	Suspension sway
Damping factor ζ ($\times 10^{-3}$)	\	4.971	5.263	5.000	5.004	4.109
Time constant T ($\times 10^{-4}$ sec)	\	6.3820	5.6149	2.0813	1.1295	0.7606
Gain K ($\times 10^{-7} \frac{\text{deg}}{\text{sec}^2 \cdot \text{A}}$)	11×10^7	8.635	6.299	-8.973	0.287	5.576

The system dynamic model can then be written as:

$$G_p(s) = \frac{K_0}{s^2} + \sum_{i=1}^n \frac{K_i}{(T_i s)^2 + 2\zeta_i T_i s + 1} \left(\frac{\text{deg}}{\text{A}} \right), \quad (2.2)$$

where n is the number of dominant resonant modes.

2.2 System Model Used in Simulation

Although the FEA result is available, the noise and disturbance data were not available. From the analysis in the last section, it is seen that the servo writer system actually has a similar behavior to a single actuator system in a HDD. In the following design procedure, an open source benchmark problem [3] of HDD control is used as an example plant. This problem is developed by a technical committee on Nano-Scale Servo (NSS) system of IEE Japan. Figure 2.8 is the frequency response (input: voltage; output: track number) of the dynamic system in the benchmark problem.

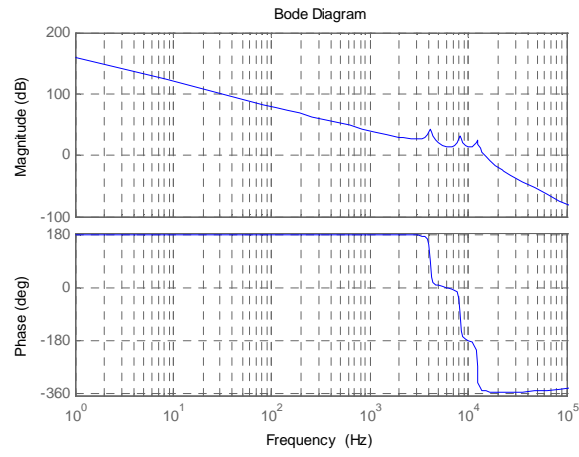


Figure 2.8: Frequency response of the dynamic model used in simulation.

Chapter 3

Robust High Precision Tracking Control for Single Spiral Writing

In this chapter, we study the position control problem in writing one stroke of spiral servo patterns.

3.1 Trajectory Design

Typical spiral writing speed is between 2 and 6 inches per second. Assume that we are performing spiral writing to a 3.5-inch disk, with an effective distance from OD to ID of 1.7 inches. Table 3.1 summarizes the parameters used in this report.

Table 3.1: Spiral writing parameters.

Parameters	Values
Spiral writing speed	5 inch/s
Maximum acceleration of the writer head	500 inch/s ²
Sampling frequency	26400 Hz
Sector number	220
Track density	100 kTPI
Track pitch	2.54×10^{-7} m

Recall that the process of moving the head from OD to ID contains three trajectory regions as defined in Fig. 3.1.

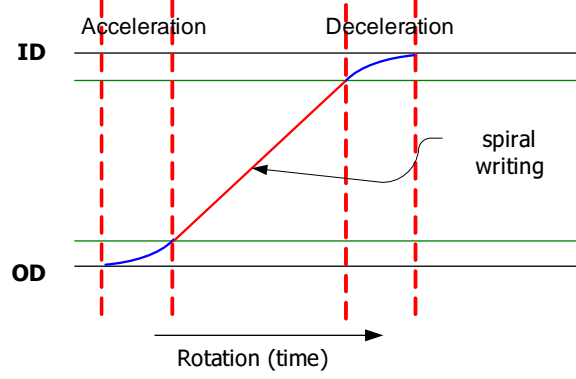


Figure 3.1: The three regions for the head to move from OD to ID.

During acceleration, to maximize the effective spiral writing region without evoking the vibration modes of the dynamic system, we apply the following Structural Vibration Minimized Acceleration Trajectory (SMART) [4]:

$$\begin{aligned}
 y(t) &= (6y_f - 3v_f t_f + \frac{a_f t_f^2}{2}) \left(\frac{t}{t_f}\right)^5 + (-15y_f + 7v_f t_f - a_f t_f^2) \left(\frac{t}{t_f}\right)^4 \\
 &\quad + (10y_f - 4v_f t_f + \frac{a_f t_f^2}{2}) \left(\frac{t}{t_f}\right)^3 \\
 v(t) &= (30y_f \frac{1}{t_f} - 15v_f + \frac{5a_f t_f}{2}) \left(\frac{t}{t_f}\right)^4 + (-60y_f + 28v_f t_f - 4a_f t_f) \left(\frac{t}{t_f}\right)^3 \\
 &\quad + (30y_f \frac{1}{t_f} - 12v_f + \frac{3a_f t_f}{2}) \left(\frac{t}{t_f}\right)^2 \\
 a(t) &= (120y_f \frac{1}{t_f^2} - 60v_f \frac{1}{t_f} + 10a_f) \left(\frac{t}{t_f}\right)^3 + (-180y_f \frac{1}{t_f^2} + 84v_f \frac{1}{t_f} - 12a_f) \left(\frac{t}{t_f}\right)^2 \\
 &\quad + (60y_f \frac{1}{t_f^2} - 24v_f \frac{1}{t_f} + 3a_f) \left(\frac{t}{t_f}\right)^1,
 \end{aligned} \tag{3.1}$$

where the initial conditions are set to $a(0) = 0$, $v(0) = 0$, $y(0) = 0$ ¹, the end conditions are assigned as $a(N) = a_f = 0$, $v(N) = v_f = \text{constant spiral writing speed}$, $y(N) = y_f = \text{start position of the effective spirals}$, and N is the length of the acceleration trajectory. Based on minimizing the jerk (the rate of change in acceleration),

¹The position is normalized w.r.t. the center of the OD seed track.

the above trajectory is shown to greatly suppress the high harmonics of the actuator acceleration [4].

When entering the effective spiral writing region, the write heads maintain the constant speed and print the servo patterns on the disk. In the deceleration region, spiral writing is not performed. The deceleration portion of the trajectory can hence be made as aggressive as possible, by applying the maximum deceleration. Figure 3.2 summarizes the proposed trajectory profile for moving the servo writer head from OD to ID.

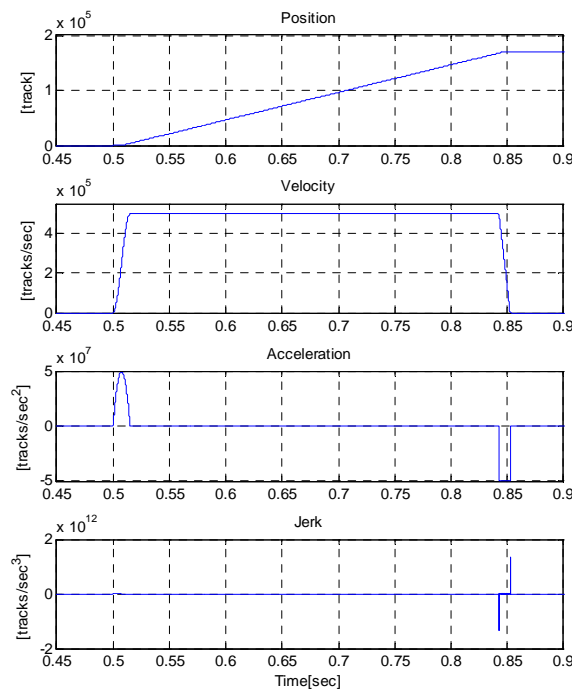


Figure 3.2: Desired trajectory profile for moving the head from OD to ID.

3.2 Overall Controller Structure

The proposed position control structure is shown in Fig. 3.3. $G_p(z^{-1})$ is the full order discrete time plant model. The output $y(k)$ is the position of the write head. The system is subjected to measurement noise plus input and output distur-

bances. A disturbance observer (DOB) is constructed to enforce robust input/output behavior by canceling the effects of disturbances and modeling errors. Three notch filters (or, more generally, plant shaping filters) are selected to attenuate the first three dominating resonant modes. The DOB loop is then stabilized by a PD type feedback controller². In tracking control, feedback signal alone provides limited tracking precision. A feed-forward zero phase error tracking controller $G_{ZPET}(z^{-1})$ [5] is constructed to achieve perfect tracking during the constant speed spiral writing.

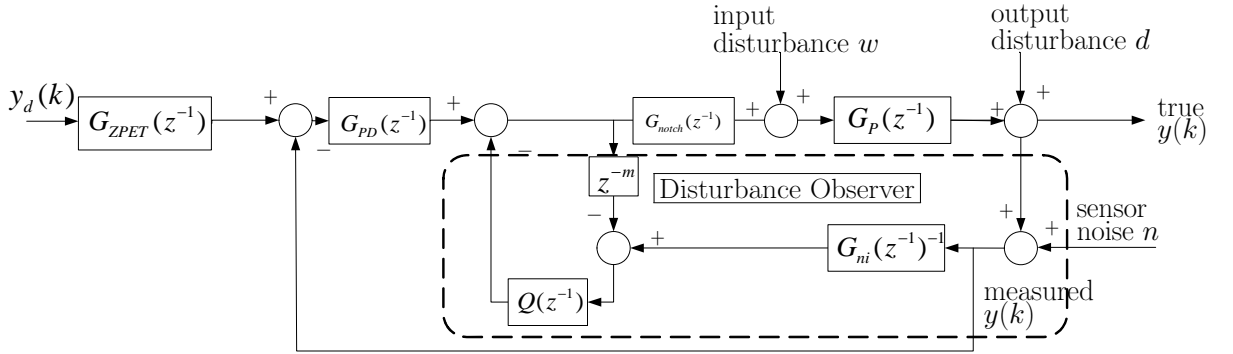


Figure 3.3: Proposed controller structure for single spiral writing.

3.3 Disturbance Observer Design

3.3.1 Review of Standard DOB

The standard discrete disturbance observer (DOB) will be reviewed here briefly. Further discussions can be found in [6, 7, 8].

3.3.1.1 Standard Structure

Consider a plant $G_p(s)$, with a zero order hold equivalence $G_p(z^{-1})$, and a low-order nominal model³ $G_n(z^{-1}) = z^{-m}G_{ni}(z^{-1})$. A standard digital DOB can be constructed as shown in Fig. 3.4, where $Q(z^{-1})$ is a so-called Q-filter that usually

²A PD controller is used here instead of a more general PID controller, since the DOB provides the I action already.

³For the DOB design, we intentionally factorize out the delay terms z^{-m} . $G_{ni}(z^{-1})$ has a relative degree of 0 and will be acting as the nominal plant for DOB inverse.

has a low-pass structure in tracking control, $G_{ni}(z^{-1})^{-1}$ is the inverse of the nominal plant without delays, $u(k)$, $w(k)$, $c(k)$, $y(k)$, and $n(k)$ are respectively the control input, the plant input disturbance, the compensation signal, the plant output, and the measurement noise.

The compensation signal $c(k)$ is designed, by constructing the DOB, to approximate and cancel the disturbance $w(k)$. To see this point, notice first that the signal $\hat{w}(k)$ is expressed by, in the operator notation,

$$\hat{w}(k) = G_{ni}(z^{-1})^{-1} [G_p(z^{-1})(u(k) + w(k)) + n(k)] - z^{-m}u(k). \quad (3.2)$$

A stable inverse model $G_n(z^{-1})^{-1}$ is needed in the above signal processing. If $G_n(z^{-1})$ has minimal phase, its inverse can directly be assigned, if not, stable inversion techniques such as the ZPET method⁴ [9] should be applied. In the servo track writer system, the nominal model is usually selected as the rigid bode model, to avoid instability in the inverse nominal model $G_{ni}(z^{-1})^{-1}$, and to simplify the design of other feedback and feed-forward controllers.

In the low frequency region, the plant $G_p(z^{-1})$ can be well approximated by its nominal model $G_n(z^{-1})$, i.e., $G_p(z^{-1}) \approx G_n(z^{-1}) = z^{-m}G_{ni}(z^{-1})$. Eq. (3.2) then becomes

$$\hat{w}(k) \approx z^{-m}w(k) + G_{ni}(z^{-1})^{-1}n(k). \quad (3.3)$$

If in addition the sensor noise $n(k)$ is small, the above equation is further simplified to

$$\hat{w}(k) \approx z^{-m}w(k) = w(k - m), \quad (3.4)$$

which implies that $\hat{w}(k)$ is a good estimate of the disturbance $w(k)$. In reality, the influence of $n(k)$ can not be ignored. The low-pass filter $Q(z^{-1})$ is constructed to form the final compensation signal $c(k)$. Adding the negative of $c(k)$ into the control input, we accomplish the disturbance rejection.

The properties of DOB can also be shown rigorously in the transfer function domain. Notice first that Fig. 3.4 can be transformed to its equivalent forms in Fig.

⁴We will discuss in detail about this in Section 3.4.

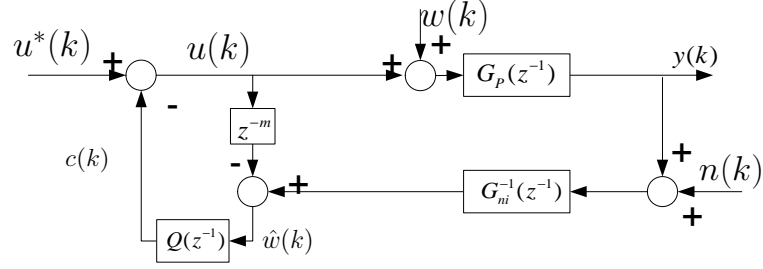


Figure 3.4: Block diagram of the standard digital DOB.

3.5 and Fig. 3.6. From Fig. 3.6, it is straightforward to derive the following transfer functions from $u^*(k)$, $n(k)$, and $w(k)$ to the output $y(k)$:

$$G_{u^*y}(z^{-1}) = \frac{G_p(z^{-1}) G_{ni}(z^{-1})}{G_{ni}(z^{-1}) + (G_p(z^{-1}) - G_{ni}(z^{-1}) z^{-m}) Q(z^{-1})} \quad (3.5)$$

$$G_{ny}(z^{-1}) = \frac{-G_p(z^{-1}) Q(z^{-1})}{G_{ni}(z^{-1}) + (G_p(z^{-1}) - G_{ni}(z^{-1}) z^{-m}) Q(z^{-1})} \quad (3.6)$$

$$G_{wy}(z^{-1}) = \frac{G_p(z^{-1}) G_{ni}(z^{-1}) (1 - Q(z^{-1}) z^{-m})}{G_{ni}(z^{-1}) + (G_p(z^{-1}) - G_{ni}(z^{-1}) z^{-m}) Q(z^{-1})}. \quad (3.7)$$

The output can thus be expressed as, in the operator notation:

$$y(k) = G_{u^*y}(z^{-1}) u^*(k) + G_{wy}(z^{-1}) w(k) + G_{ny}(z^{-1}) n(k). \quad (3.8)$$

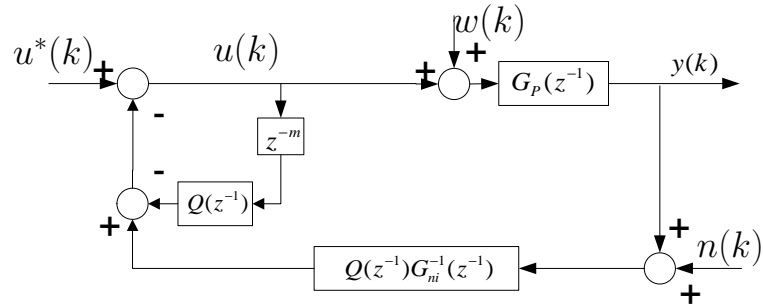


Figure 3.5: Equivalent form 1 of the standard DOB.

In the low frequency region where $Q(z^{-1}) \approx 1$, if the delay is small so that $(1 - z^{-m})G_{ni} \approx 0$, then $G_{wy}(z^{-1}) \approx 0$ in Eq. (3.7), $G_{ny}(z^{-1}) \approx -1$ in Eq. (3.6), and $G_{u^*y}(z^{-1}) \approx G_n$ in Eq. (3.5). The disturbance $w(k)$ is thus attenuated and the entire DOB loop behaves like the nominal plant $G_n(z^{-1})$. This observation makes it possible

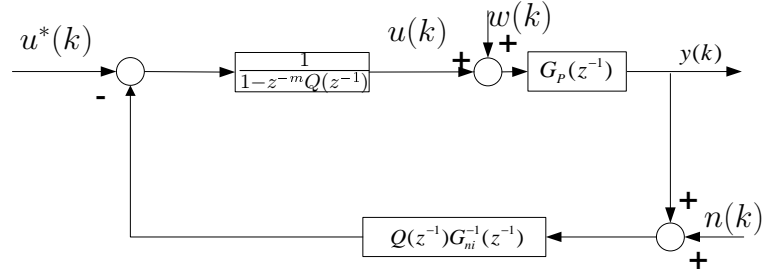


Figure 3.6: Equivalent form 2 of the standard DOB.

to design other feedback or feed-forward controllers simply based on the low order nominal model. In the high frequency region where $Q(z^{-1}) \approx 0$, DOB is essentially inactive, therefore $G_{u^*y}(z^{-1}) \approx G_p(z^{-1})$, $G_{wy}(z^{-1}) \approx G_p(z^{-1})$, and $G_{ny}(z^{-1}) \approx 0$, which indicates that the high frequency sensor noise is attenuated or it does not enter the DOB loop.

The above analysis indicates that selection of the Q-filter plays an important role in DOB performance. Two types of properties in $Q(z^{-1})$ are essential: the cut-off frequency and the high frequency roll off. In servo track writers, sensors are usually accurate and measurement noise contributes little to the output error. It is therefore preferred that the cut-off frequency of $Q(z^{-1})$ be chosen as high as possible. To analyze the effect of the high frequency roll off, we observe first from Eqs. (3.5) and (3.7), that in the region where the true plant can be well modeled by the nominal model, $1 - Q(z^{-1})$ and $Q(z^{-1})$ are approximately the sensitivity and complementary sensitivity functions of the DOB loop. As can be seen from Fig. 3.7, the high frequency roll off of the Q-filter determines the shape $Q(z^{-1})$ and $1 - Q(z^{-1})$, and hence the trade-off between DOB performance and robustness. It has been suggested [10] that the following type of Q-filter results in a disturbance observer with balanced overall properties:

$$Q(s) = \frac{3\tau s + 1}{(\tau s + 1)^3}. \quad (3.9)$$

For implementation, $Q(s)$ is discretized using the following bilinear transforma-

tion:

$$Q(z^{-1}) = Q(s) \Big|_{s=\frac{2}{T} \frac{1-z^{-1}}{1+z^{-1}}} = \frac{3\tau \frac{2}{T} (1+z^{-1})^2 (1-z^{-1}) + (1+z^{-1})^3}{\left(\tau \frac{2}{T} (1-z^{-1}) + 1+z^{-1}\right)^3}, \quad (3.10)$$

where T denotes the sampling time.

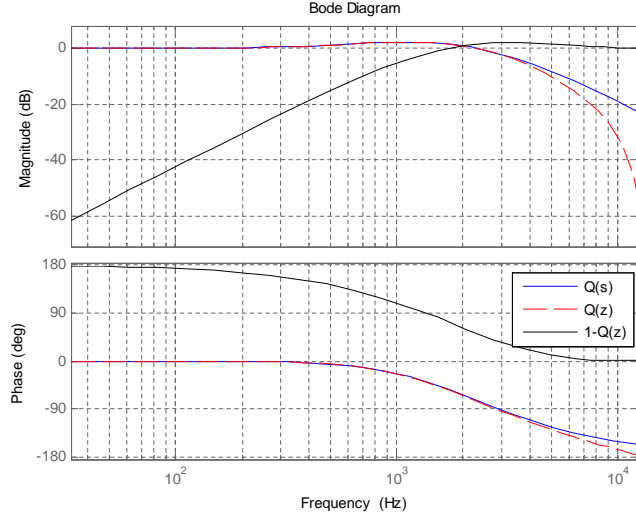


Figure 3.7: Frequency response of a Q-filter with a cut-off frequency of 2000 Hz.

3.3.1.2 Stability Robustness

When there is unmodeled dynamics in the plant, the cut-off frequency of the Q-filter should be carefully designed. Consider $G_p(z^{-1})$ as a perturbed version of the nominal model $z^{-m}G_{ni}(z^{-1})$, and the unmodeled dynamics as a multiplicative perturbation $\Delta(z^{-1})$:

$$G_p(z^{-1}) = z^{-m}G_{ni}(z^{-1}) (1 + \Delta(z^{-1})). \quad (3.11)$$

From Eq. (3.5), the closed loop characteristic polynomial is given by

$$A_c(z^{-1}) = G_{ni}(z^{-1}) + (G_p(z^{-1}) - G_{ni}(z^{-1}) z^{-m}) Q(z^{-1}) \quad (3.12)$$

Substituting Eq. (3.11) to Eq. (3.12), we have

$$A_c(z^{-1}) = G_n(z^{-1}) (z^m + \Delta(z^{-1}) Q(z^{-1})). \quad (3.13)$$

The small gain theorem gives that DOB is stable if the zeros of $G_n(z^{-1})$ are all in the unit circle and that

$$|e^{-mj\omega} \Delta(e^{j\omega}) Q(e^{j\omega})| < 1 \quad \forall \omega. \quad (3.14)$$

Eq. (3.14) holds if and only if

$$|Q(e^{j\omega})| < \frac{1}{|\Delta(e^{j\omega})|} \quad \forall \omega \quad (3.15)$$

Selection of the deterministic nominal model $G_n(z^{-1})$ has been introduced at the beginning of this section. The difficulty for maintaining stability is mainly caused by the unmodeled dynamics $\Delta(z^{-1})$. When the nominal model is selected as the rigid bode model, the ignored resonant modes will severely limit the bandwidth of Q-filter and thus the disturbance rejection capability of DOB. Figure 3.8 shows the Q-filter designed in a standard DOB for our servo track writer system. It is seen that in order to maintain the DOB stability, the Q-filter's cut-off frequency ω_c is limited to 320 Hz. To achieve a larger ω_c , we propose in the next section a new modified disturbance observer structure by shaping the plant to minimize the modeling error. This result is discussed also in detail in [11].

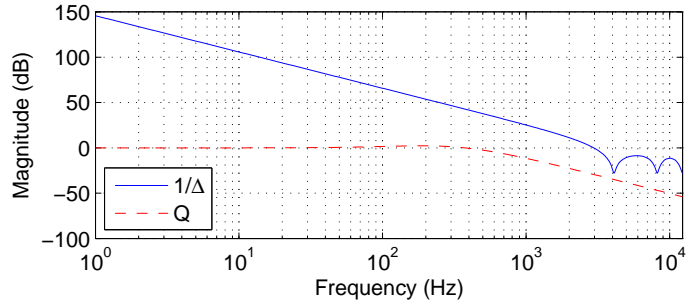


Figure 3.8: Magnitude responses of $Q(z^{-1})$ and $1/\Delta(z^{-1})$ in the standard DOB: cut-off frequency of Q-filter restricted to be below 320 Hz.

3.3.2 DOB Based on Optimal Plant Shaping

3.3.2.1 Controller Structure and Properties

Figure 3.9 shows the structure of the proposed DOB. Different from the standard form, a shaping filter $G_s(z^{-1})$ is cascaded preceding the plant $G_p(z^{-1})$. Defining the shaped plant $\bar{G}_p(z^{-1}) \triangleq G_p(z^{-1})G_s(z^{-1})$, we now have

$$\begin{aligned} G_{u^*y}(z^{-1}) &= \frac{\bar{G}_p(z^{-1})G_{ni}(z^{-1})}{G_{ni}(z^{-1}) + [\bar{G}_p(z^{-1}) - G_n(z^{-1})]Q(z^{-1})}, \\ G_{ny}(z^{-1}) &= \frac{-\bar{G}_p(z^{-1})Q(z^{-1})}{G_{ni}(z^{-1}) + [\bar{G}_p(z^{-1}) - G_n(z^{-1})]Q(z^{-1})}, \\ G_{wy}(z^{-1}) &= \frac{G_p(z^{-1})G_{ni}(z^{-1})[1 - Q(z^{-1})z^{-m}]}{G_{ni}(z^{-1}) + [\bar{G}_p(z^{-1}) - G_n(z^{-1})]Q(z^{-1})}. \end{aligned} \quad (3.16)$$

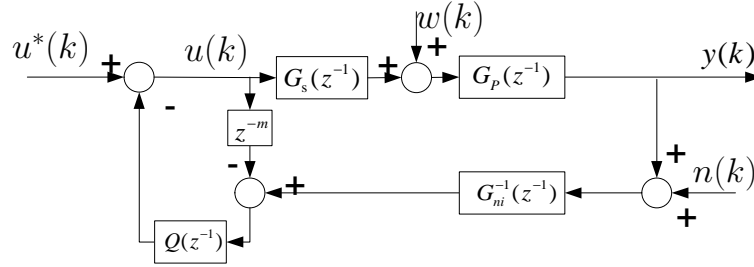


Figure 3.9: Block diagram: DOB based on optimal plant shaping.

Parallel to the analysis in Section 3.3.1, Table 3.2 can be constructed. It is seen that the modified DOB possesses all the advantages of a standard DOB, i.e., low frequency disturbance rejection, nominal model following, and high frequency sensor noise attenuation. Moreover, superior to the standard disturbance observer, the modified DOB has the following additional properties:

1. Resonance attenuation: from Table 3.2, in the high frequency region, the DOB loop behaves like $G_{u^*y}(z^{-1}) \approx \bar{G}_p(z^{-1}) = G_p(z^{-1})G_s(z^{-1})$. If a shaping filter is properly constructed, the resonance modes can then be well attenuated.
2. Enlarged disturbance rejection bandwidth: by careful design, $G_s(z^{-1})$ can actively reduce the mismatch between $\bar{G}_p(z^{-1})$ and $G_n(z^{-1})$. After optimization

of $G_s(z^{-1})$, the cut-off frequency of $Q(z^{-1})$, and thus the DOB disturbance rejection bandwidth, can be greatly enlarged.

Table 3.2: Properties of the Proposed DOB When $z^{-m} \approx 1$.

Frequency Region	Low Frequency	High Frequency
Q-filter	$Q(z^{-1}) \approx 1$	$Q(z^{-1}) \approx 0$
$G_{u^*y}(z^{-1})$	$G_{u^*y}(z^{-1}) \approx G_n(z^{-1})$	$G_{u^*y}(z^{-1}) \approx \bar{G}_p(z^{-1})$
$G_{wy}(z^{-1})$	$G_{wy}(z^{-1}) \approx 0$	$G_{wy}(z^{-1}) \approx G_p(z^{-1})$
$G_{ny}(z^{-1})$	$G_{ny}(z^{-1}) \approx -1$	$G_{ny}(z^{-1}) \approx 0$

3.3.2.2 Stability Robustness

Similar to Section 3.3.1, we have the following results for the proposed DOB structure:

The closed loop characteristic polynomial:

$$\bar{A}_c(z^{-1}) = G_{ni}(z^{-1}) + [\bar{G}_p(z^{-1}) - G_n(z^{-1})] Q(z^{-1}). \quad (3.17)$$

Let $\bar{G}_p(z^{-1})$ be subjected to multiplicative model uncertainties:

$$\bar{G}_p(z^{-1}) = G_n(z^{-1}) (1 + \bar{\Delta}(z^{-1})), \quad (3.18)$$

where

$$\bar{\Delta}(z^{-1}) = \frac{G_p(z^{-1}) G_s(z^{-1}) - G_n(z^{-1})}{G_n(z^{-1})}. \quad (3.19)$$

The stability of the modified DOB requires $G_n(z^{-1})$ to have no zeros outside the unit circle and that

$$|\bar{\Delta}(e^{j\omega}) Q(e^{j\omega})| < 1 \quad \forall \omega. \quad (3.20)$$

Equation (3.20) appears to have a similar structure with (3.14), except that here $\bar{\Delta}(z^{-1})$ is the multiplicative model uncertainty between $\bar{G}_p(z^{-1})$ and $G_n(z^{-1})$, while in the standard DOB $\Delta(z^{-1}) = [G_p(z^{-1}) - G_n(z^{-1})] / G_n(z^{-1})$. Assuming that the nominal plant model remains the same in the two cases, in the proposed DOB, by

cascading the shaping filter to the plant, we make the magnitude of $\bar{\Delta}(e^{j\omega})$, and thus that of $|\bar{\Delta}(e^{j\omega})Q(e^{j\omega})|$ smaller. Therefore, the Q-filter can have a higher cut-off frequency in the proposed method.

3.3.2.3 Shaping Filter Design

Define x as the coefficient vector to be optimized in the shaping filter. Based on the previous discussion, x should be chosen such that:

$$J(x) = \|G_s(x, e^{j\omega})G_p(e^{j\omega}) - G_n(e^{j\omega})\|_2^2 \quad (3.21)$$

is minimized over the frequency range where there is strong model mismatch between $G_p(z^{-1})$ and $G_n(z^{-1})$. For the servo track writer system, the range around the resonant modes, i.e., [1 kHz, 13 kHz], needs to be taken into the optimization.

Notice that (3.21) contains two optimization problems, the magnitude matching to minimize

$$J_1 = \left\| \|G_s(e^{j\omega})G_p(e^{j\omega})\| - \|G_n(e^{j\omega})\| \right\|_2^2,$$

and the phase matching to minimize

$$J_2 = \left\| \text{phase}(G_s(e^{j\omega})G_p(e^{j\omega})) - \text{phase}(G_n(e^{j\omega})) \right\|_2^2.$$

For the magnitude matching, when resonances are the main sources of model mismatch, the structure of the shaping filter can be a combination of several notch filters, i.e.,

$$G_s(s) = \prod_{i=1}^m \frac{s^2 + 2\zeta_i\bar{\omega}_i s + \bar{\omega}_i^2}{s^2 + 2x_i\bar{\omega}_i s + \bar{\omega}_i^2}, \quad (3.22)$$

where ζ_i and $\bar{\omega}_i$ are the damping ratio and center frequency of the i^{th} resonance, and are obtained through system identification⁵. x_i ($x_i > \zeta_i$ for notch filters) is the notch coefficient that needs tuning. It is easier to perform optimization in the continuous time domain, by noting that the magnitude response at frequency ω_k is given by

$$|G_s(j\omega_k)| = \prod_{i=1}^m \frac{\sqrt{(\bar{\omega}_i^2 - \omega_k^2)^2 + 4\bar{\omega}_i^2\omega_k^2\zeta_i^2}}{\sqrt{(\bar{\omega}_i^2 - \omega_k^2)^2 + 4\bar{\omega}_i^2\omega_k^2x_i^2}}. \quad (3.23)$$

⁵The resonance frequency may change with respect to the temperature. In practice, adaptive notch filter is assigned by using temperature sensors.

Taking the log to normalize the unit to dB, we have

$$f_k(y) = 20 \log |G_s(j\omega_k)| = M_k - 10 \sum_{i=1}^m \log \{A_k + B_k y_i\}, \quad (3.24)$$

where $y_i = x_i^2$, $A_k = (\bar{\omega}_i^2 - \omega_k^2)^2$, $B_k = 4\bar{\omega}_i^2 \omega_k^2$, and $M_k = 10 \sum_{i=1}^m \log \{A_k + B_k a_i^2\}$. Noting that $\log |G_s(j\omega)G_p(j\omega)| = \log |G_s(j\omega)| + \log |G_p(j\omega)|$, we transform the magnitude matching in (3.21) to the following simplified version:

$$\min_{y \in \mathbb{R}^m} \|f(y) - 20(\log |G_n(j\omega)| - \log |G_p(j\omega)|)\|_2^2 \quad (3.25)$$

$$\text{subject to } \zeta_i^2 < y_i < 1, \quad i = 1, 2, \dots, m \quad (3.26)$$

where $f(y)$, $\log |G_n(j\omega)|$, and $\log |G_p(j\omega)|$ are column vectors with each of their elements being the magnitude response at selected frequency points. This is a nonlinear least squares problem. When the number of parameters to be identified is small, performing direct line search to y_i over the region $[\zeta_i^2, 1]$, i.e., evaluating the objective function at a variety of parameter values in the input space, can lead us to the minimal. Otherwise, nonlinear programming based on combined gradient and Newton methods can be applied. The latter can be performed in MATLAB using the nonlinear least squares data fitting function *lsqcurvefit*.

The $G_s(s)$ derived above is then digitized to $G_s(z^{-1})$, using MATLAB's *c2d* function with the pole zero match method (*matched*). The phase match problem can now be addressed by adding delay z^{-j} or advance elements z^j into $G_s(z^{-1})$, and examining directly the phase difference between $G_s(e^{j\omega})G_p(e^{j\omega})$ and $G_n(e^{j\omega})$ in the frequency response. For causality, when z^j is needed, instead of modifying $G_s(z^{-1})$, z^{-j} can be added to $G_n(z^{-1})$, since minimizing the phase difference between $z^j G_s(z^{-1})G_p(z^{-1})$ and $G_n(z^{-1})$ is equivalent to minimizing the phase difference between $G_s(z^{-1})G_p(z^{-1})$ and $z^{-j} G_n(z^{-1})$. However, to achieve a DOB with high performance, the delay elements should not be too many [6].

We now apply the proposed shaping method to our system. The solid line and the dotted line in Fig. 3.10 show the frequency responses of the plant and the nominal plant. There are three dominant resonant modes in the plant. The shaping filter is the product of three notch filters. In the magnitude matching, the notch coefficients

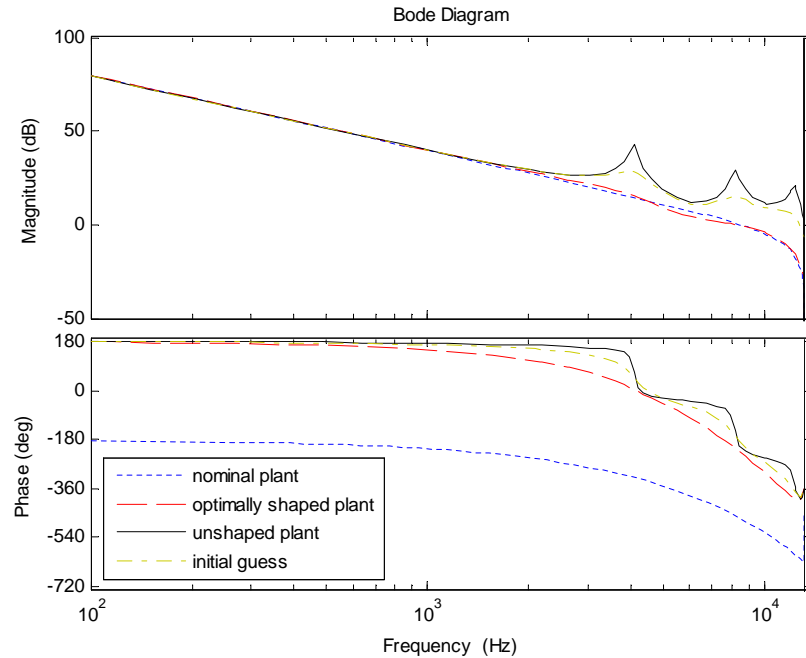


Figure 3.10: Frequency responses of the plant, the nominal plant, the optimally shaped plant, and the plant with initial shaping filter guess.

are all initialized at the value of 0.1. It can be observed, that the resulting optimal solution $[0.403, 0.316, 0.364]^T$ achieves good matching between the shaped plant and the nominal plant. Figure 3.11 presents the frequency response of the final optimal shaping filter.

Figure 3.12 shows graphically the robust stability conditions in the proposed DOB structure. Compared with Fig. 3.8, the high frequency model uncertainties have been greatly reduced, and the Q-filter cut-off frequency can now increase from 320 Hz to as large as 2000 Hz.

The shaping filter brought some phase drop starting at around 1kHz. Phase matching was thus performed after the magnitude matching. Note that digital disturbance observers accept only integer amounts of delays. Two delay steps were added to achieve the good phase match up to about 3 kHz, which is high enough for normal servo operation. The nominal plant finally developed a form as a double integrator

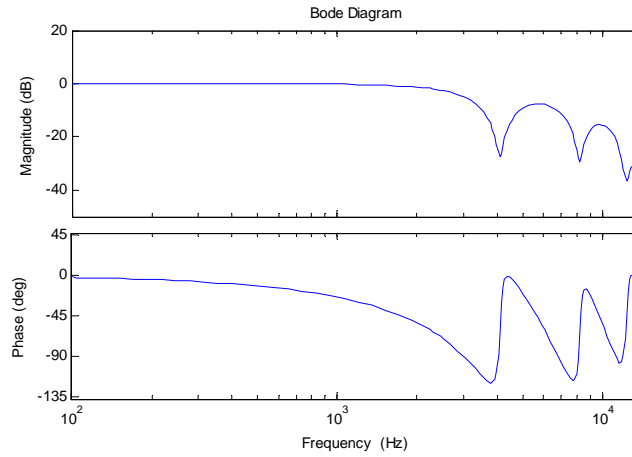


Figure 3.11: Frequency response of the optimal shaping filter.

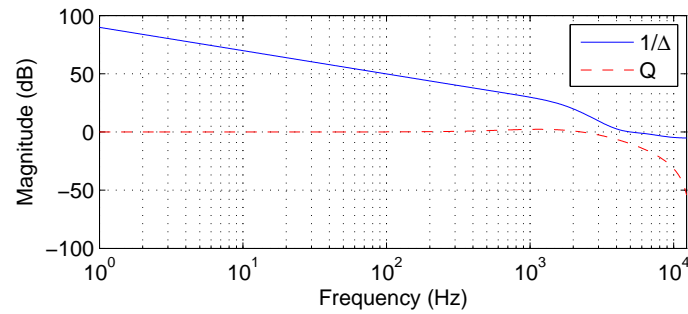


Figure 3.12: Magnitude responses of $Q(z^{-1})$ and $1/\Delta(z^{-1})$ in the proposed DOB: Q-filter cut-off frequency can expand to as large as 2000 Hz.

with two delay steps, i.e.,

$$G_n(z^{-1}) = z^{-2} \frac{K_0 T_s^2 z^{-1} (1 + z^{-1})}{2(1 - z^{-1})^2}. \quad (3.27)$$

3.3.2.4 Optimal Plant Shaping From the View Point of Nominal Model

Through simple block diagram transformation, it can be shown that the proposed DOB is equivalent to the form in Fig. 3.13.

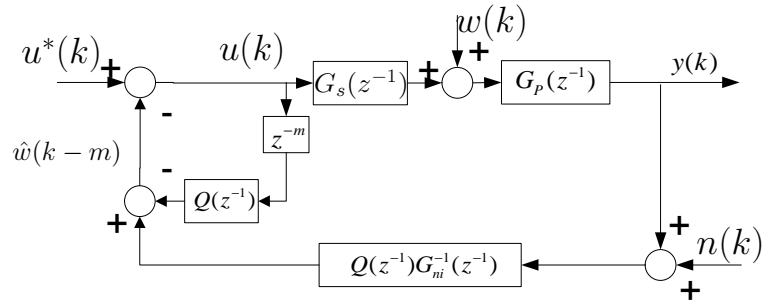


Figure 3.13: Equivalent form one of the proposed DOB.

The block diagram in Fig. 3.13 can be additionally transformed to that shown in Fig. 3.14, via the transformation in Fig. 3.15.

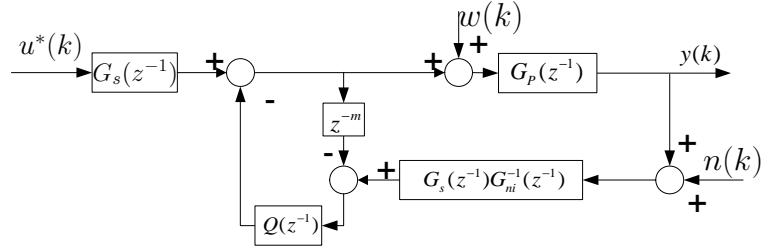


Figure 3.14: Equivalent form two of the proposed DOB.

From Fig. 3.14, we see that the proposed DOB can be alternatively viewed from the nominal model aspect. It is now observed that our design is optimal in the sense of not only shaping the actual plant, but also providing a stable inverse of a nominal model that contains the plant resonances. Notice that simply inverting the full-order plant model $G_p(z^{-1})$ will not provide a stable $G_{ni}^{-1}(z^{-1})$, while in our optimal design, $Q(z^{-1})G_{ni}^{-1}(z^{-1})$ is always stable in Fig. 3.14.

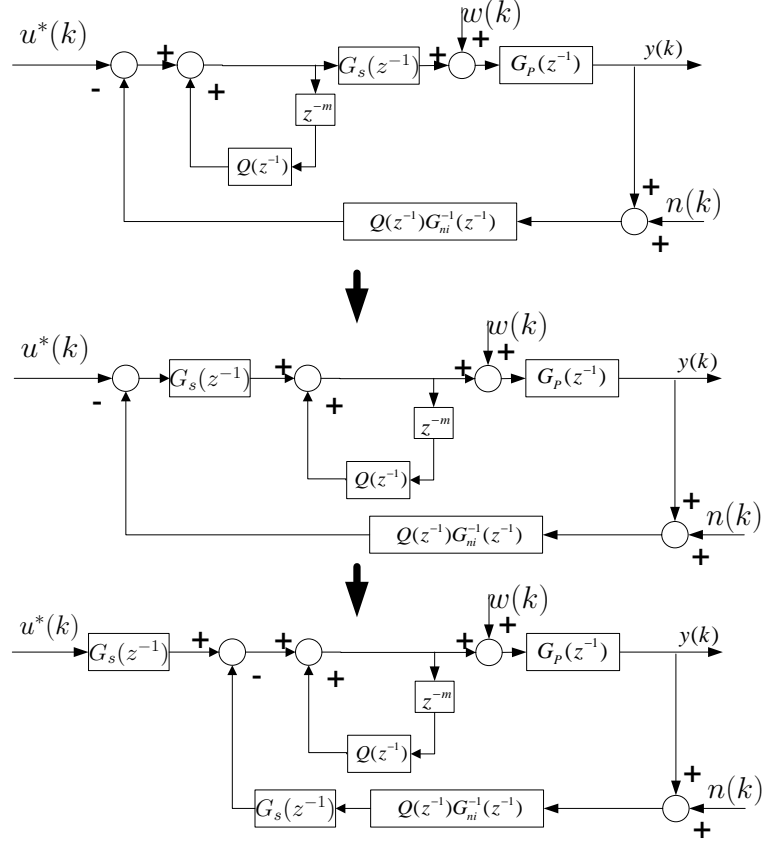


Figure 3.15: Equivalent loop transformation of the proposed DOB.

3.4 Zero Phase Error Tracking for Improved Spiral Writing

Recall our overall controller structure in Fig. 3.16, where the optimal DOB discussed in the previous section is applied as an inner loop controller, and a PD type feedback controller $G_{PD}(z^{-1})$ serves as the closed loop servo controller to meet the stability and the bandwidth requirements. The disturbance observer makes the DOB loop behave like the nominal plant $G_n(z^{-1})$, and remain robust in the presence of low frequency disturbances. Therefore, below the cut-off frequency of $Q(z^{-1})$, the feedback closed loop transfer function will be close to

$$G_{closed}(z^{-1}) = \frac{G_n(z^{-1})G_{PD}(z^{-1})}{1 + G_n(z^{-1})G_{PD}(z^{-1})}. \quad (3.28)$$

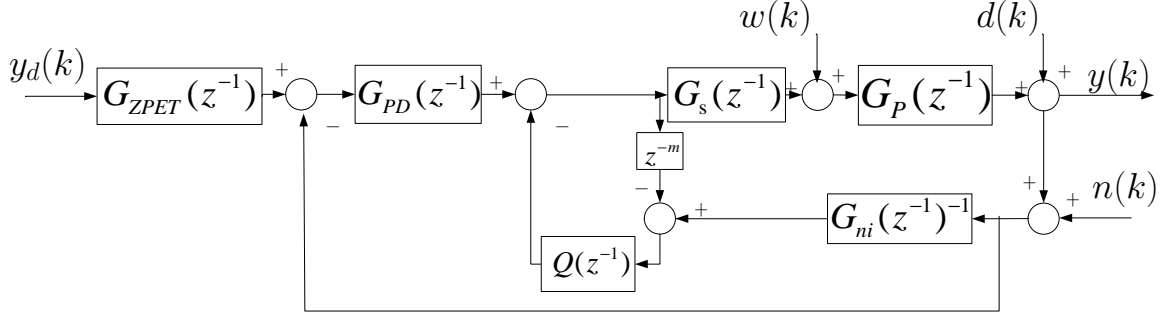


Figure 3.16: Overall controller structure applying the DOB based on optimal plant shaping.

Based on $G_{closed}(z^{-1})$, a feed-forward zero phase error tracking [9] controller can now be constructed to achieve high performance tracking. To begin our design, partition first the overall feedback loop transfer function by

$$G_{closed}(z^{-1}) = \frac{z^{-d}B_c(z^{-1})}{A_c(z^{-1})} = \frac{z^{-d}B_c^-(z^{-1})B_c^+(z^{-1})}{A_c(z^{-1})}, \quad (3.29)$$

where $B_c^-(z^{-1})$, $B_c^+(z^{-1})$ and $A_c(z^{-1})$ denote respectively the non-cancellable numerator part, the cancellable numerator part, and the stable closed loop characteristic polynomial. The ZPET controller is then given by

$$G_{ZPET}(z^{-1}) = z^d \frac{A_c(z^{-1})B_c^-(z)}{B_c^+(z^{-1})B_c^-(1)^2}, \quad (3.30)$$

where $B_c^-(z)$ is derived by replacing every z^{-1} in $B_c^-(z^{-1})$ with z , and $B_c^-(1)$ is obtained through replacing every z^{-1} in $B_c^-(z^{-1})$ with 1.

The overall transfer function from $y_d(k)$ to $y(k)$ is therefore given by

$$G_{overall}(z^{-1}) = G_{ZPET}(z^{-1})G_{closed}(z^{-1}) = \frac{B_c^-(z^{-1})B_c^-(z)}{B_c^-(1)^2}. \quad (3.31)$$

We observe that:

- The stable poles and cancellable zeros in $G_{closed}(z^{-1})$ are canceled by the ZPET controller.
- The product of the complex conjugate pair $B_c^-(z)B_c^-(z^{-1})$ remains zero phase in the entire frequency domain. By the additional scaling of $1/B_c^-(1)^2$, we achieve

a DC gain of 0 dB.

In the spiral writing case, the unstable zero $z = -1$ in the nominal plant (Eq. (3.27)) is preserved under feedback control, and $B_c^-(z^{-1}) = 1 + z^{-1}$. We thus have

$$G_{overall} = \frac{(1 + z^{-1})(1 + z)}{4},$$

which is a zero-phase low-pass filter. It has been shown [5] that if the desired position trajectory is either a step signal or a ramp signal, the above ZPET control algorithm achieves asymptotic perfect tracking .

The transfer function in Eq. (3.30) is not directly implementable. Denoting s as the order of $B_c^-(z)$, we instead add $d + s$ steps of delays to Eq. (3.30) and apply the $d + s$ step-advanced version of the reference trajectory, as shown in Fig. 3.17.

$$y_d(k + d + s) \longrightarrow \boxed{\frac{z^{-s} A_c(z^{-1}) B_c^-(z)}{B_c^+(z^{-1}) B_c^-(1)^2}} \longrightarrow \boxed{G_{closed}(z^{-1})} \longrightarrow y(k)$$

Figure 3.17: Practical implementation of the ZPET control algorithm.

There have been several suggested methods to enhance the performance of ZPET controllers [12, 13]. The common cost of enhancing the tracking performance is the increased liability on the future knowledge of the desired trajectory. Here we apply one of the methods [12] that appears to be simple and efficient. The so called E-filter method [12] cascades an additional zero phase filter to the original ZPET controller to enlarge the bandwidth of the overall transfer function $G_{overall}(z^{-1})$. The E filter takes the form

$$G_{Efilter}(z^{-1}) = \frac{(\beta_e + z^{-1})(\beta_e + z)}{(1 + \beta_e)^2}, \quad (3.32)$$

where $0 < \beta_e < 1$ is a design parameter that determines the filter bandwidth. Guidelines of selecting β_e are provided in [12].

Plotting the magnitude responses of $G_{overall}(z^{-1})$ in Fig. 3.18, we observe that either with or without the E-filter, the overall system behaves like a unity function in a wide low frequency range, and the E-filter simply further extends the cut-off frequency of $G_{overall}(z^{-1})$.

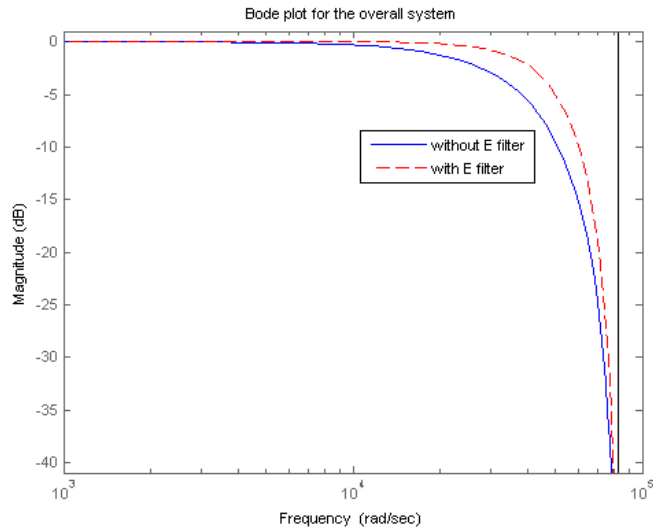


Figure 3.18: Magnitude responses of $G_{overall}(z^{-1})$ with and without E-filter (sampling frequency: 26400 Hz).

3.5 Simulation Results

In this section, the proposed control structure is applied to single spiral writing. We present first the deterministic reference tracking result, to show the efficacy of our trajectory design and the system's tracking ability. The servo performance under various external disturbance, such as the pivot friction, the repeatable runout (RRO), the sensor noise, etc, will then be presented in Section 3.5.2, where we will examine the robustness of the systems, and especially, the performance of the disturbance observer.

3.5.1 Deterministic Tracking

Figures 3.19 and 3.20 present the servo performance when no external disturbance is added to the system. It is observed that the tracking errors have been well controlled to be below 0.02 track pitch (1 track pitch = $0.25\mu m$). Moreover, we have achieved zero tracking error in the constant speed spiral writing region, and smooth settling during the acceleration (less than 0.001 track pitch). As has been discussed in Section

3.1, no spirals are written in the deceleration region. Therefore, errors around 0.85 sec (although already smaller than 0.02 track pitch) do not influence the spiral pattern quality. No chattering appears in the tracking error, indicating the high frequency resonant modes are not provoked.

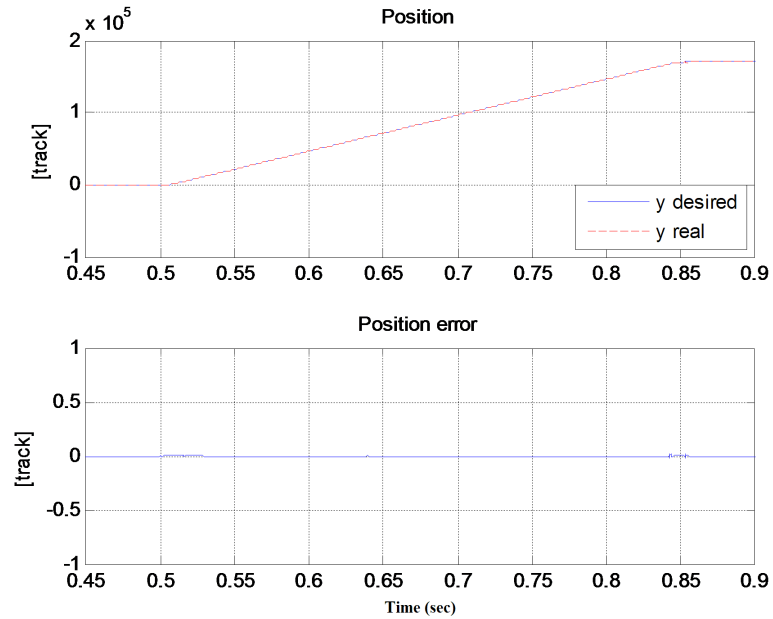


Figure 3.19: Simulated position tracking result.

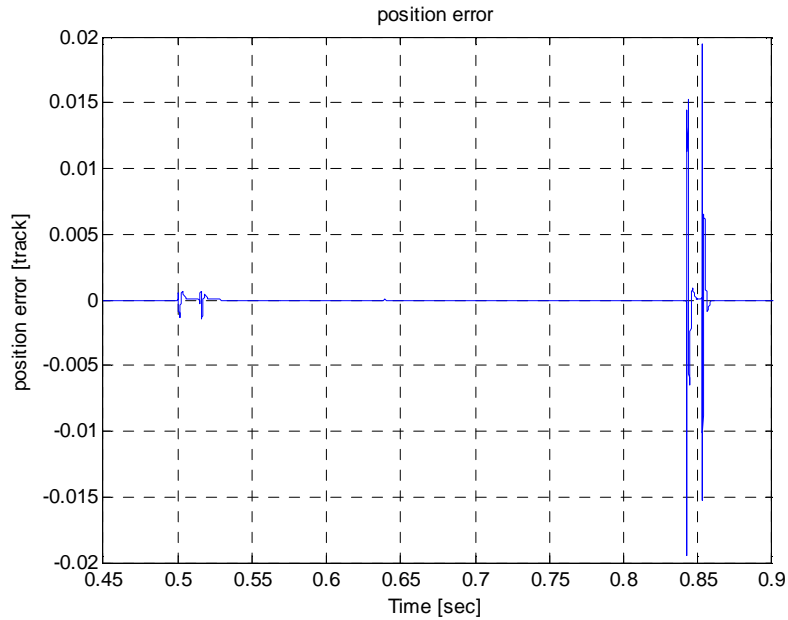


Figure 3.20: Simulated position tracking error.

3.5.2 Tracking in the Presence of External Disturbances

In spiral servo writing, a group of actuators work together to achieve multi-disk writing at the same time. The motion of each actuator and the spindle vibration of each disk can all cause disturbance to the system. There also exist friction induced input torque disturbances, sensor noise, and repeatable output disturbances. In this section, we consider the above uncertainties and introduce disturbances at the input side and the output side of the plant. Detailed knowledge about the disturbances in servo track writing is currently unavailable either in literature or in experiments. What we employ in our simulation is the disturbance profile from a realistic benchmark HDD track following problem [3]. Servo track writers are much more precise machines than HDDs. Our simulation can therefore be regarded as a worst case analysis of what may happen in actual servo track writing.

Let us revisit the single spiral writing control structure in Fig. 3.21. The modeled input disturbance w is a zero mean white noise with standard derivation $\sigma = 1 \times 10^{-4}$ amp. The disturbances d at the output side is composed of two parts: a zero

mean colored disk flutter disturbance η ($\sigma = 1.7\%$ track pitch) and a repeatable output disturbance ν whose energy is concentrated at 100 Hz, 200 Hz, and 300 Hz. Additionally, a zero mean white measurement noise n ($\sigma = 1.5\%$ track pitch) is added to the system. Figure 3.22 and 3.23 show respectively the spectra of the repeatable disturbances and the non-repeatable disturbance signal.

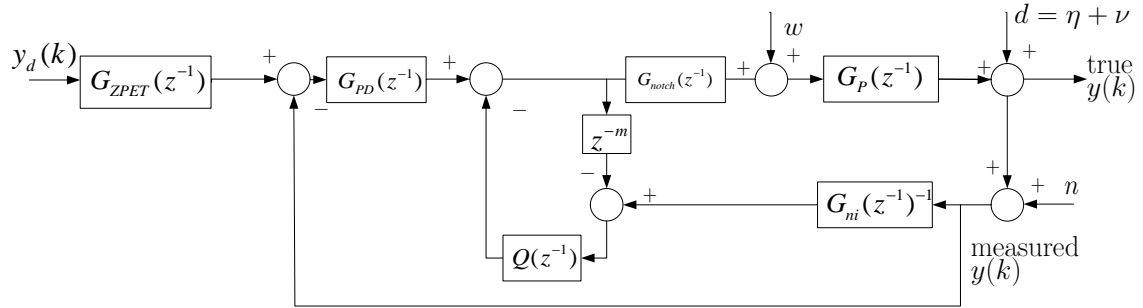


Figure 3.21: Block diagram of the proposed control structure in noisy environments

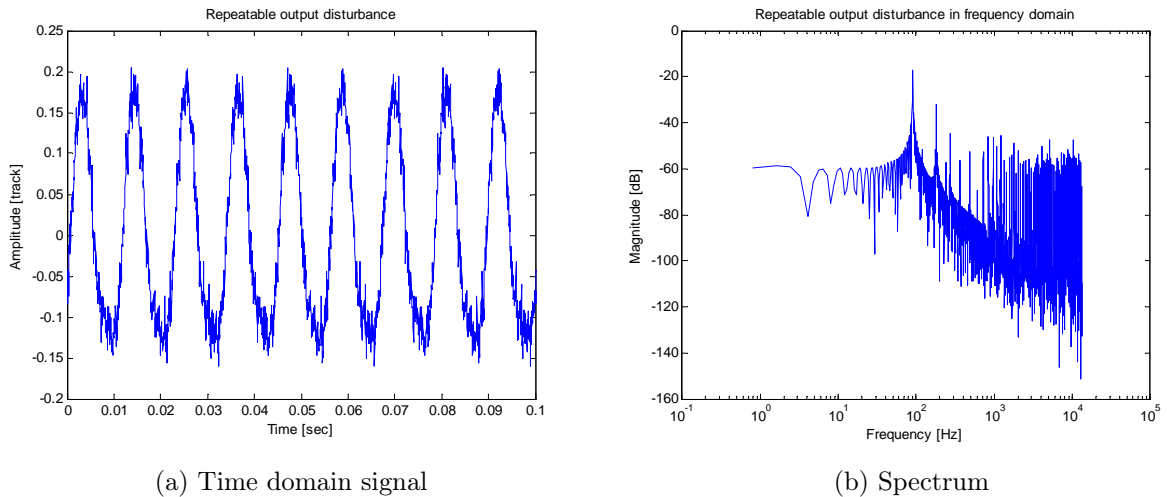


Figure 3.22: The repeatable output disturbance data.

The tracking results are shown in Fig. 3.24. It is seen the tracking error is kept to be below 0.1 track pitch (TP). Figure 3.25 further shows the disturbance rejection performance in the frequency domain. The disturbance below 1000 Hz has been greatly reduced compared to the case without the DOB.

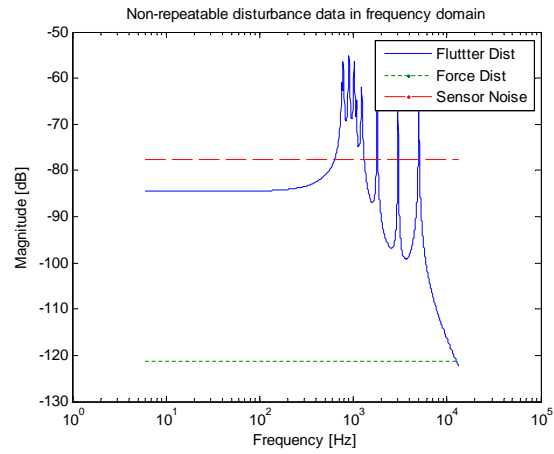


Figure 3.23: Spectrum of the non-repeatable disturbance.

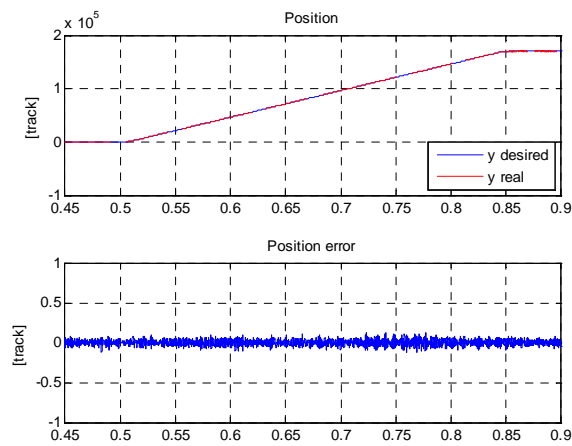


Figure 3.24: Simulated position tracking result in a noisy environment.

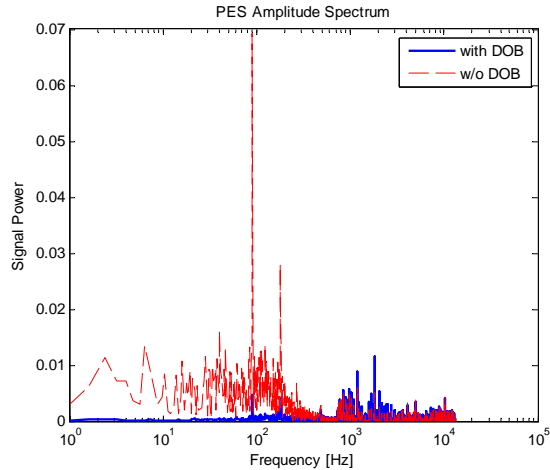


Figure 3.25: Spectrum of the simulated position tracking error in a noisy environment.

To see further the advantages of the proposed high bandwidth DOB based on plant shaping method, we perform another simulation with the proposed DOB replaced by the standard DOB⁶. Figure 3.26 shows the tracking errors in the two cases. The maximum error dropped from 0.21 TP in the standard DOB to 0.13 TP in the proposed DOB, implying a 38% improvement. The standard deviation of the error decreased from 0.0518 to 0.0319. A spectrum analysis of the error signals further reveals the superiority of the proposed algorithm. We can see from Fig. 3.27, that compared to the standard DOB, the proposed algorithm had a much higher disturbance rejection band. Errors below 2000 Hz were greatly reduced due to the high cut-off frequency of Q-filter.

Finally, the magnitude responses from the input disturbance to the plant output are shown in Fig. 3.28. The response in the proposed DOB exhibits a much deeper magnitude drop in the middle frequency region, resulting in a larger disturbance rejection capability. A small high frequency region gets slightly amplified, due to the *waterbed* effect that it is theoretically impossible for the closed loop transfer function to simultaneously have small magnitudes at all frequencies. However, since the low frequency disturbance dominates, overall the error is better attenuated.

⁶The feedback controller in this case is the same PD controller cascaded with several notch filters.

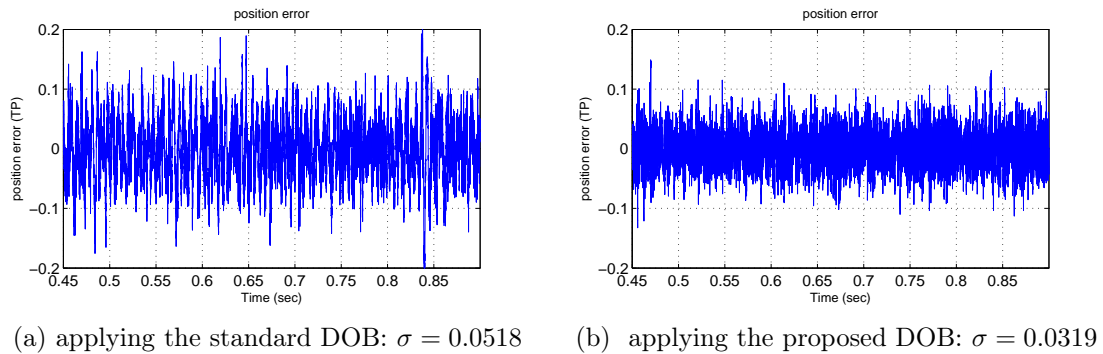


Figure 3.26: Time traces of the tracking errors.

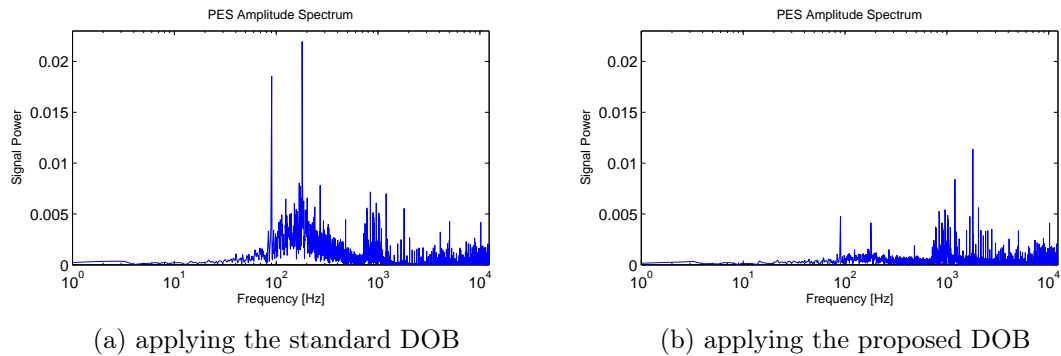


Figure 3.27: Frequency spectra of the tracking error.

3.6 Summary

In this chapter, we have discussed the control of writing the servo patterns in one spiral. A robust high performance tracking control scheme has been developed that combines good tracking and disturbance rejection performances. In reality, hundreds of spirals need to be written on one disk. The above task is thus repeated until enough spirals are written for the self servo writing process in the next HDD manufacturing stage. The repetitive nature of spiral writing makes it possible to further increase the tracking accuracy by using customized control algorithms. We will show in the next chapter that this can be (simply) achieved by further modifying the control structure presented in this chapter. The key idea is to 'learn' from the errors in the previous spirals and make some adjustment in the new control input, and the tool we use is

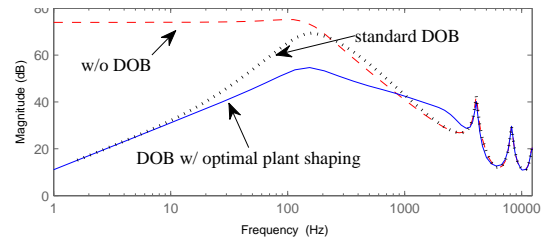


Figure 3.28: Magnitude response from input disturbance to plant output.

iterative learning control.

Chapter 4

Iterative Learning Control for Multiple Spiral Writing

In this chapter, the control of writing several spirals is discussed. There are typically over 400 spirals to write for one disk. After finishing writing one spiral, the servo writer heads rotate back to the initial position at the outer diameter (OD) and wait for the correct timing to write the next stroke. In consequence, the heads move back and forth between the inner diameter (ID) and OD, sweeping the disk by following the same trajectory.

Iterative learning control (ILC) is a popular and effective feed-forward control technique to improve tracking performance in systems that perform a task for multiple times. The key concept in ILC is that one additional domain is introduced due to the repetition of the same task. Errors in the previous trials¹ can be used for the design of the current trial input signal. To begin our discussion, we introduce the following

¹A trial is sometimes also called an iteration/repetition, or an execution.

notations for the control scheme in Fig. 4.3.

j :trial number

k :time index within each iteration

$u_j(k)$:(general) control input at the j^{th} iteration

$\eta_j(k)$:non-repeatable output disturbance at the j^{th} iteration

$w_j(k)$:non-repeatable input disturbance at the j^{th} iteration

$n_j(k)$:non-repeatable sensor noise at the j^{th} iteration

$\nu(k)$:iteration independent disturbance (lumped at the output side)

We now present the idea of 'learning' in Fig. 4.1 and Fig. 4.3. In writing the first stroke of spiral, i.e., in the first trial, the ZPET plus optimal DOB algorithm is used, and the system works the same as that in Chapter 3. Starting from the second trial, ILC concept is applied. As shown in Fig. 4.2 and Fig. 4.3, the closed loop is considered as the new generalized plant with a transfer function $G_{closed}(z^{-1})$. The input $u_j(k)$ to $G_{closed}(z^{-1})$ is composed of two signals: $u_{j-1}(k)$ from the last trial plus a filtered version of the last trial error, which is defined as

$$e_{j-1}(k) = y_d(k) - y_{j-1}(k).$$

In the error filtering process, $L(z^{-1})$ is the so-called learning filter and $Q_{ILC}(z^{-1})$ is a zero-phase low-pass filter to improve the system robustness. If $L(z^{-1})$ is set to be zero, no correction will be made to the input signal, and in each iteration the system works the same as that controlled by the ZPET plus optimal DOB controllers. By a proper design of $L(z^{-1})$ and $Q_{ILC}(z^{-1})$, tracking error can be effectively reduced as the task repeats. Notice that ILC here is introduced as an enhancing control technique. The existing feedback system does not need to be broke down to change any functions or hardware initialization routines. Figure 4.4 presents an equivalent form of Fig. 4.3 where the input to the closed loop system is decomposed to the ZPET initialization plus the learned information from the previous trials.

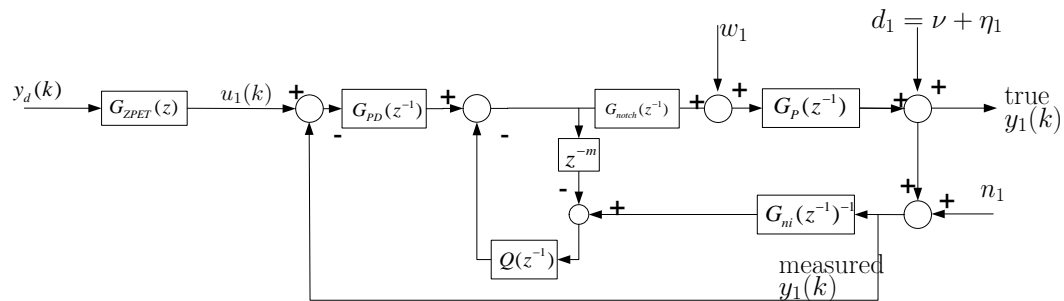
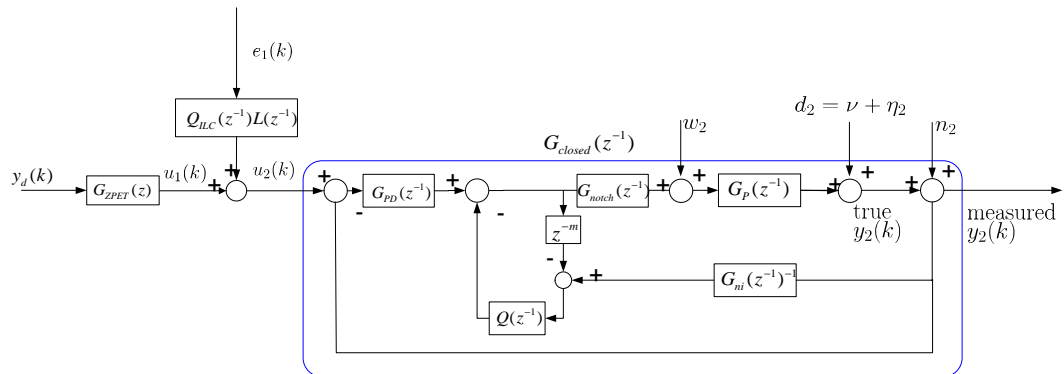
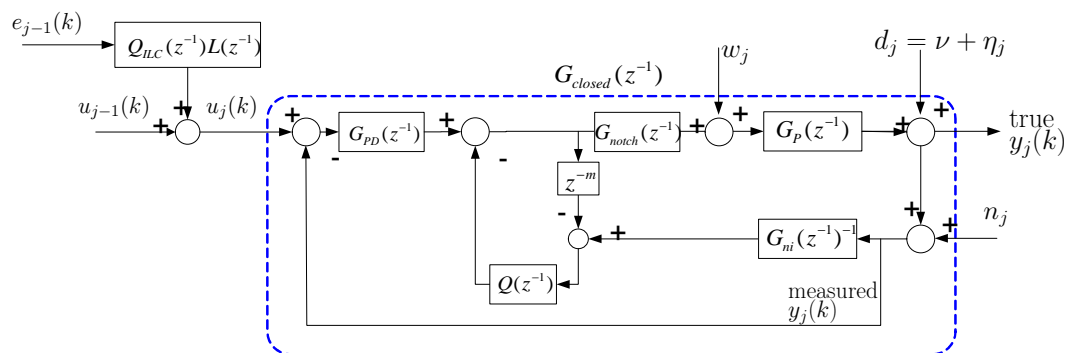


Figure 4.1: Block diagram of ILC combined with ZPET control: the first trial

Figure 4.2: Block diagram of ILC combined with ZPET control: 2nd trial.Figure 4.3: Block diagram of ILC combined with ZPET control: j^{th} trial ($j > 1$)

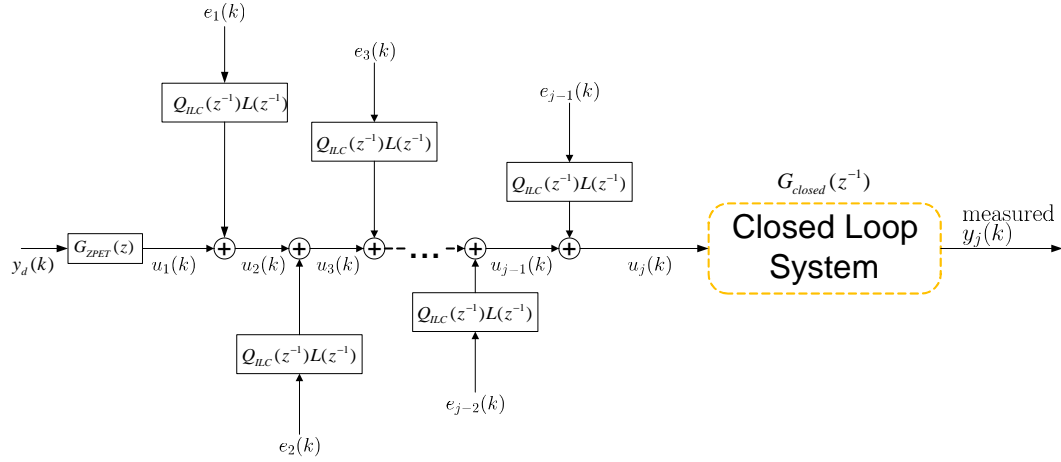


Figure 4.4: Equivalent form of the proposed ILC algorithm.

4.1 Trajectory Design

The trajectory of multiple spiral writing differs from that of single spiral writing only in how the heads behave after reaching the inner diameter. As has been discussed in Section 3.1, spirals are only written in the constant speed region when moving the heads from OD to ID. The trajectory for moving the heads back to OD can be made as aggressive as possible. As a demonstration, we apply the maximum acceleration and deceleration when setting the head to the initial position, and assume the allowable maximum speed to be twice the spiral writing speed. Figure 4.5 shows the trajectory for one full movement from OD to ID and then back to OD.

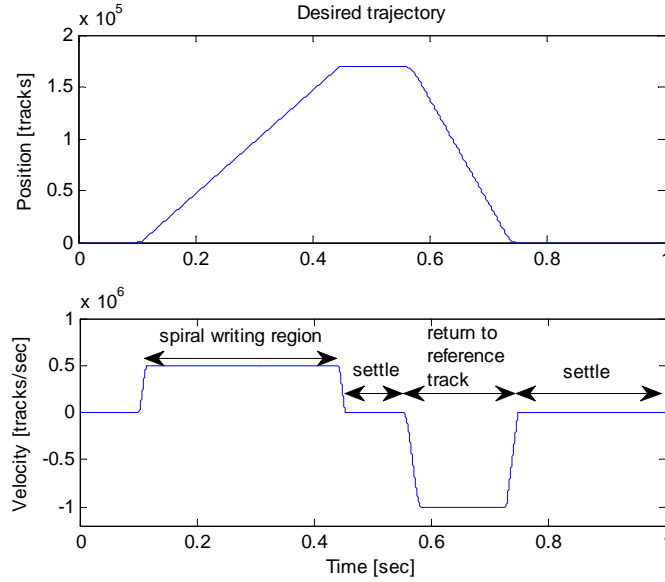


Figure 4.5: Reference trajectory for one trial.

4.2 Iterative Learning Control Design

4.2.1 Control Law Derivation

Consider the general case that a feedback loop has been constructed with a feedback controller $C(z^{-1})$ as shown in Fig. 4.6. Assume the process starts from zero initial condition at each iteration, i.e., $y_j(0) = 0 \forall j$ and $u_j(k) = 0 \forall k < 0, \forall j \geq 1$. The transfer functions from $u_j \rightarrow y_j$, $w_j \rightarrow y_j$, $d_j \rightarrow y_j$, and $n_j \rightarrow y_j$ are given by²

$$T_u = \frac{G_p C}{1 + G_p C}; \quad T_w = \frac{G_p}{1 + G_p C}; \quad T_d = \frac{1}{1 + G_p C}; \quad T_n = \frac{-G_p C}{1 + G_p C}. \quad (4.1)$$

The input-output relation is thus given by

$$\text{true output: } y_j = T_u u_j + T_w w_j + T_d (\nu + \eta_j) + T_n n_j, \quad (4.2)$$

$$\text{measured output: } m_j = T_u u_j + T_w w_j + T_d (\nu + \eta_j) + T_n n_j + n_j. \quad (4.3)$$

²To simplify the notations, we drop the time index k and the z -domain index z when no confusion is generated.

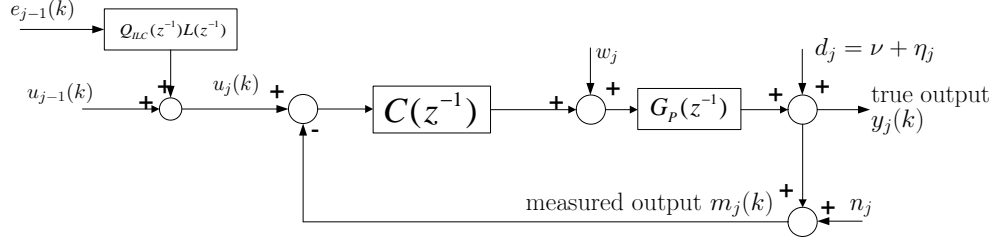


Figure 4.6: Equivalent block diagram of ILC combined with ZPET control

Let $y_d(k)$ denote the desired position trajectory, we can then define at iteration j the true error $e_j^o(k) = y_d(k) - y_j(k)$, and the measured error $e_j(k) = y_d(k) - m_j(k)$. Notice that there exist the following relationship between the true and the measured signals

$$m_j = y_j + n_j; \quad e_j = e_j^o + n_j. \quad (4.4)$$

Only m_j is available for the controller design. The ILC control law for the closed loop is constructed by

$$u_{j+1}(k) = u_j(k) + Q_{ILC} (z^{-1}) L(z^{-1}) e_j(k). \quad (4.5)$$

The following theorem holds for the proposed ILC algorithm. The proof is provided in Appendix A.

Theorem 4.1. *In the proposed ILC control structure, the error caused by the repetitive disturbance ν can be perfectly attenuated, and the true error is updated by*

$$e_{j+1}^o = (1 - T_u Q_{ILC} L) e_j^o + T_w (w_j - w_{j+1}) + T_d (\eta_j - \eta_{j+1}) + T_n (n_j - n_{j+1}) - T_u Q_{ILC} L n_j. \quad (4.6)$$

In Eq. (4.6), the non-repeatable error terms $w_j - w_{j+1}$, $\eta_j - \eta_{j+1}$, and $n_j - n_{j+1}$ are bounded zero mean stochastic processes. Learning only happens in the term $(1 - T_u Q_{ILC} L) e_j^o$. The best we can do is to let the first term on the right hand side be as close to zero as possible. It appears clearly the ideal compensator would be $L = T_u^{-1}$, and $Q_{ILC} = 1$. In that case, the maximum convergence rate is achieved, i.e., the repeatable error goes to zero at the second iteration. However, this can hardly be realized in practice due to the fact that an exact stable plant inverse is usually

unavailable. Here we propose to apply the zero phase error tracking idea to the ILC compensator design. Similar to the ZPET design in Section 3.4, we first partition $T_u(z^{-1})$ as follows

$$T_u(z^{-1}) = \frac{z^{-d}B_c(z^{-1})}{A_c(z^{-1})} = \frac{z^{-d}B_c^-(z^{-1})B_c^+(z^{-1})}{A_c(z^{-1})},$$

where $B_c^-(z^{-1})$ and $B_c^+(z^{-1})$ are respectively the uncancellable and cancellable parts in the numerator.

To approximate $T_u^{-1}(z^{-1})$, the learning filter can then be designed as

$$L(z^{-1}) = z^d \frac{A_c(z^{-1})B_c^-(z)}{B_c^+(z^{-1})B_c^-(1)^2}. \quad (4.7)$$

In our spiral writing project, the assign of $L(z^{-1})$ is greatly simplified since $T_u(z^{-1})$ is the same as $G_{closed}(z^{-1})$ in Section 3.4. Therefore, the ZPET controller $G_{ZPET}(z^{-1})$ can be directly assigned as the learning filter $L(z^{-1})$. Additionally, the implementation of ILC is also the same as that in Section 3.4, namely, adding delays to $L(z^{-1})$ to make it realizable and sending the several step-advanced version of the reference trajectory as the input of $L(z^{-1})$. The proposed algorithm can be regarded either an extension of the general two degree of freedom control structure or as an ILC algorithm that applies ZPET as its initialization.

4.2.2 Stability and Robust Stability

In the following analysis, we assume the trajectory cycle length $N \rightarrow \infty$, so that z-domain and frequency domain analysis is rigorous.

Using the control structure described in the previous section, and noting that in our spiral writing project, $T_u(z^{-1}) = G_{closed}(z^{-1})$, we have

$$L(z^{-1})T_u(z^{-1}) = L(z^{-1})G_{closed}(z^{-1}) = \frac{B_c^-(z^{-1})B_c^-(z)}{B_c^-(1)^2} = \frac{(1+z^{-1})(1+z)}{4}. \quad (4.8)$$

The above transfer function is a low-pass filter. $Q_{ILC}(z^{-1})$ is also a zero-phase low pass filter. Therefore $1 - L(z^{-1})Q_{ILC}(z^{-1})T_u(z^{-1})$ in Eq. (4.6) satisfies

$$|1 - L(e^{-j\omega T})Q_{ILC}(e^{-j\omega T})T_u(e^{-j\omega T})| < 1 \quad \forall \omega > 0. \quad (4.9)$$

Notice that Eq. (4.6) describes a first order dynamic system. Equation (4.9) therefore indicates that the proposed ILC structure is asymptotically stable.

Design of FIR Zero Phase Low-pass Filters There are different methods for designing zero phase filters. One popular way is to use the command *filtfilt* in MATLAB. This method performs a time inverse to the data, and applies a non-zero-phase filter twice. Alternatively, we can apply the following design of a non-causal FIR zero-phase low-pass filter. A simple candidate of such a filter is

$$Q_{ILC}(z^{-1}) = \frac{(1+z^{-1})(1+z)}{4}. \quad (4.10)$$

To have extra freedom on the cut-off frequency, we add additional zero pairs to the above filter. The transfer function for such a zero pair can be given by

$$H(z^{-1}) = \frac{1-2\beta z^{-1}+z^{-2}}{2-2\beta} \cdot \frac{1-2\beta z+z^2}{2-2\beta}. \quad (4.11)$$

A negative β in the above equation results in four zeros on the left hand side of the unit circle. $\frac{1-2\beta z+z^2}{2-2\beta}$ is the complex conjugate of $\frac{1-2\beta z^{-1}+z^{-2}}{2-2\beta}$, resulting in $H(z^{-1})$ to have zero phase in the entire frequency range.

Combining Eq. (4.10) and Eq. (4.11) yields

$$Q_{ILC}(z^{-1}) = \frac{(1+z^{-1})(1+z)}{4} \cdot \prod_{i=0}^M \left(\frac{1-2\beta_i z^{-1}+z^{-2}}{2-2\beta_i} \cdot \frac{1-2\beta_i z+z^2}{2-2\beta_i} \right). \quad (4.12)$$

Figure 4.7 is the pole zero map of a low-pass filter following the above design process. Two pairs of zeros are added with $\beta_1 = -0.3$ and $\beta_2 = -0.7$ respectively. Figure 4.8 shows the corresponding frequency response.

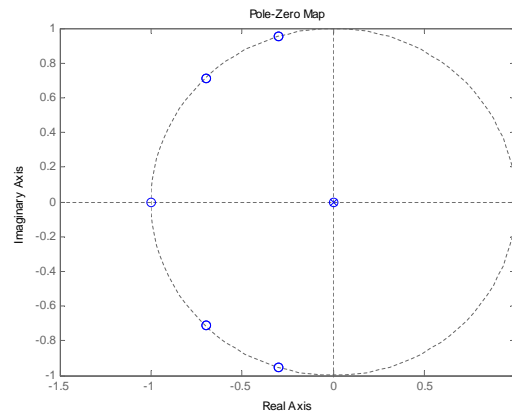


Figure 4.7: Pole zero map of a zero phase low-pass filter.

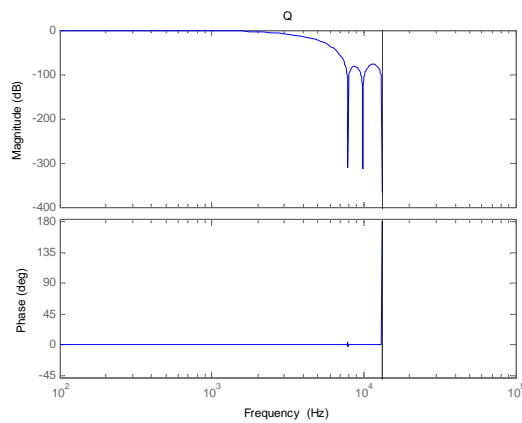


Figure 4.8: Simulated frequency response of a low-pass filter.

4.3 Simulation Results

We now implement the proposed algorithm to the servo track writing process. Similar to Chapter 16, we first consider the deterministic tracking performance, then discuss the case with external disturbances.

4.3.1 Deterministic Tracking

Figure 4.9 shows the stacked time trace of the tracking errors in the first fourteen spirals when no external disturbance is present ($w_j = 0$, $\nu = 0$, $\eta_j = 0$, $n_j = 0$). Each trial lasts one second. It is observed that after four trials we have more than eighty percent reduction in the maximum error magnitudes. In Fig. 4.10, the ILC stability and convergence are graphically presented from the propagation of the l_2 and l_∞ norms of the tracking errors.

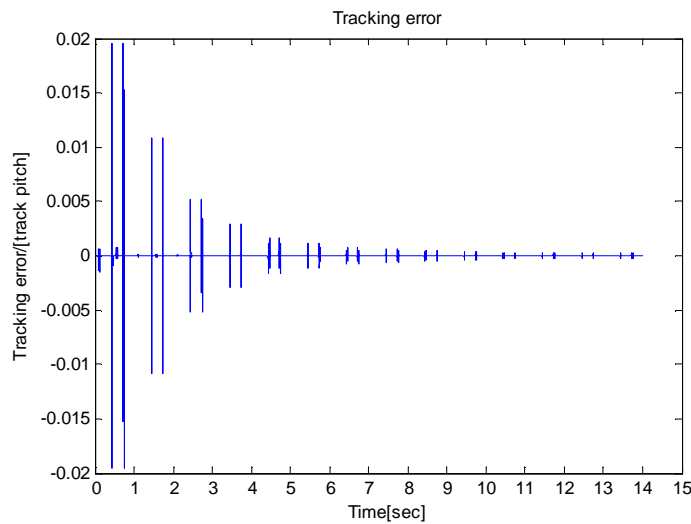


Figure 4.9: Simulated tracking errors in the deterministic reference tracking: each trial lasts one second, the time traces of all the 14 trials are stacked into a long vector to demonstrate the tracking performance.

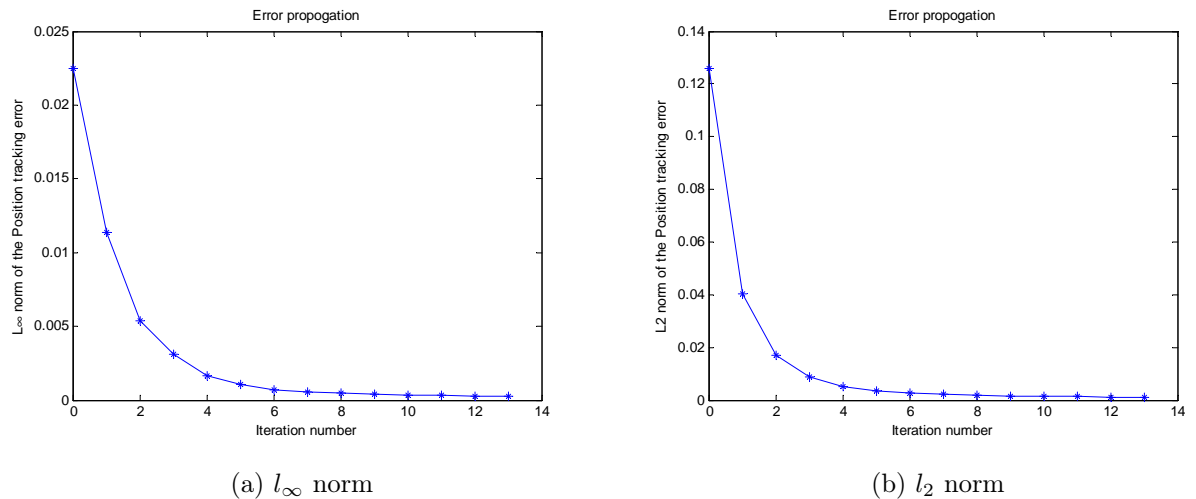


Figure 4.10: Norms of the simulated tracking errors in the deterministic reference tracking.

In deterministic tracking control, the ultimate aim is finding the signal input to the closed loop system such that the output of the plant follows the desired trajectory as close as possible. If the process is highly repeatable, ILC can be applied in the actual process. Even when the control task is non-repetitive, if exact models of plant and disturbances are available, we can always perform ILC simulations first and then apply the 'learned' control signal to the actual system.

4.3.2 Tracking in the Presence of External Disturbances

Applying the same disturbance profile as in Section 3.5.2, and using the control law discussed in Section 4.2, we get the tracking results as shown in Fig. 4.11 and Fig. 4.12. It can be seen that although the repetitive disturbances at the frequencies around 100 Hz (RRO center frequency), 200 Hz (RRO center frequency), 1000 Hz (plant modeling error frequency), and 2000 Hz (plant modeling error frequency) are well attenuated by the proposed ILC structure, the overall performance enhancement is not very apparent. This is due to the fact that the applied disturbance profile contains too much non-repeatable components, namely, the term $T_w(w_j - w_{j+1}) + T_v(\eta_j - \eta_{j+1}) + T_n(n_j - n_{j+1}) - T_u Q_{ILC} L n_j$ in Eq. (4.6) takes a dominant role.

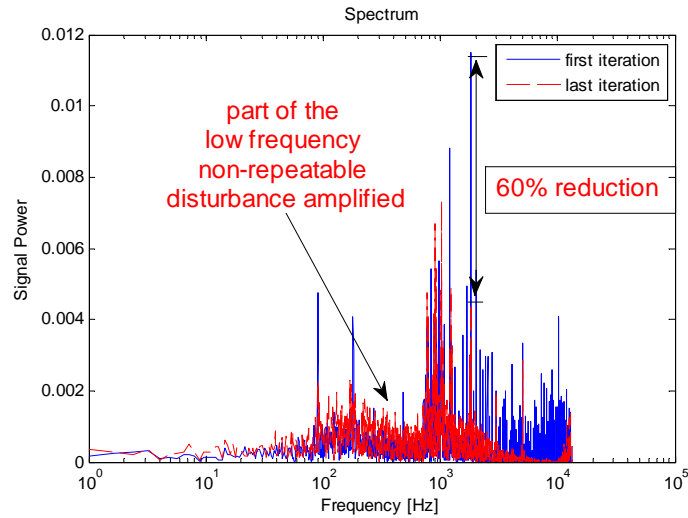


Figure 4.11: Comparison of the simulated error spectra: first and 30th iteration.

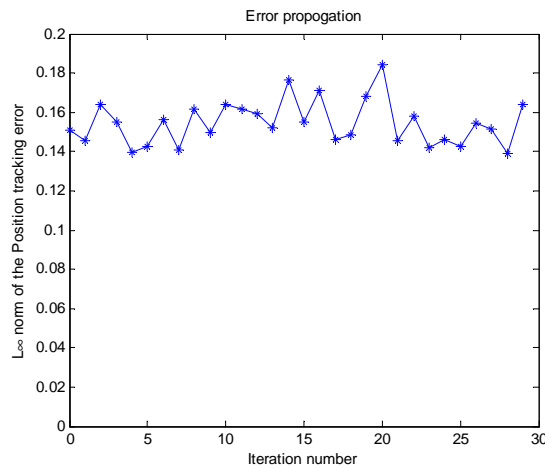


Figure 4.12: l_{∞} norms of the simulated tracking errors with external disturbance.

Recall that we applied a HDD disturbance profile in our simulation, which can only be a worst case approximation of the servo track writer system. In Fig. 4.13, we make the amplitude of the repetitive disturbance 10 times larger than that in the previous disturbance profile. The proposed ILC then results in apparent performance enhancement.

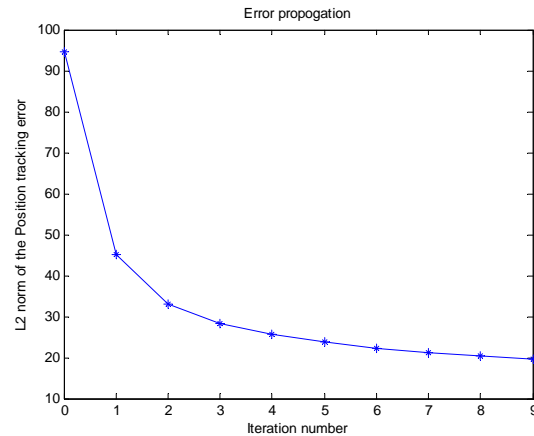


Figure 4.13: Simulated tracking errors with enhanced repetitive disturbance.

We have seen in this section that non-repetitive disturbances reduces the tracking accuracy. This is indeed a notorious problem in iterative learning control, as has been pointed out in [14, 15]. We will look into this problem in the next chapter.

4.4 Summary

In this chapter, ILC has been proposed to combine with the ZPET plus optimal DOB control structure. Simulation results show apparent improvements in the deterministic reference tracking, where the tracking error decreases monotonically as the task repeats. The algorithm also works well when the major disturbance is repetitive over iterations.

The presence of high levels of non-repeatable disturbance deteriorates the ILC performance. Depending on the actual servo track writer hardware characteristics, minor modifications may be required. In the next chapter, strategies will be made to reduce the learning speed of those non-repetitive disturbances. It will be shown that some careful modifications to the ILC control law will result in effective learning even when non-repetitive disturbance dominates.

Chapter 5

Robust Iterative Learning Control

In the last chapter, ILC in the presence of external disturbances has been simulated in the spiral writing project. As it has been shown, the algorithm worked fine if the repetitive disturbance dominates (Fig. 4.13). However, if non-repetitive disturbances take the leading parts, conventional ILC would not work well (Fig. 4.12). In this chapter, we try to reduce the influence of non-repetitive disturbances in ILC.

5.1 Multi-iteration ILC

Recall the ILC error update equation:

$$\begin{aligned}
 e_{j+1}^o &= (1 - T_u Q_{ILC} L) e_j^o + T_w (w_j - w_{j+1}) + T_d (\eta_j - \eta_{j+1}) \\
 &\quad + T_n (n_j - n_{j+1}) - T_u Q_{ILC} L n_j \\
 &= (1 - T_u Q_{ILC} L) e_j^o + (T_w w_j + T_d \eta_j + T_n n_j - T_u Q_{ILC} L n_j) \\
 &\quad - (T_w w_{j+1} + T_d \eta_{j+1} + T_n n_{j+1}).
 \end{aligned} \tag{5.1}$$

On the right hand side of the above equation, the third term comes from the disturbance in the current iteration, and can be attenuated only by the feedback loop design; the second term is resulted from the ILC update (see also the proof in Appendix A):

$$u_{j+1}(k) = u_j(k) + Q_{ILC} (z^{-1}) L (z^{-1}) e_j(k). \tag{5.2}$$

To reduce the influence of the non-repetitive term $T_w w_j + T_\nu \eta_j + T_n n_j - T_u Q_{ILC} L n_j$ in ILC, the simplest way would be to recognize its zero-mean property and perform an averaging process as follows:

Step 1, run the system for M ($M > 1$) times and collect the errors in each iteration.

Step 2, calculate the mean of the collected errors over the iterations.

Step 3, apply the calculated mean values as the last trial error in ILC, and update the control law in the next iteration.

Step 4, go to step 2 and repeat until the iteration ends.

As a demonstration of writing 56 spirals, we set $M = 7$ and updated the ILC control law by the above multi-iteration averaging process. Figure 5.1 shows the resulting tracking error. We observe in Fig. 5.1a a reduction of the l_2 norm from around 5.2 to 4.8 after the first update, and a further reduction to 4.5 after a few more learning steps. Similar observations can be found in the l_∞ norm update in Fig. 5.1b.

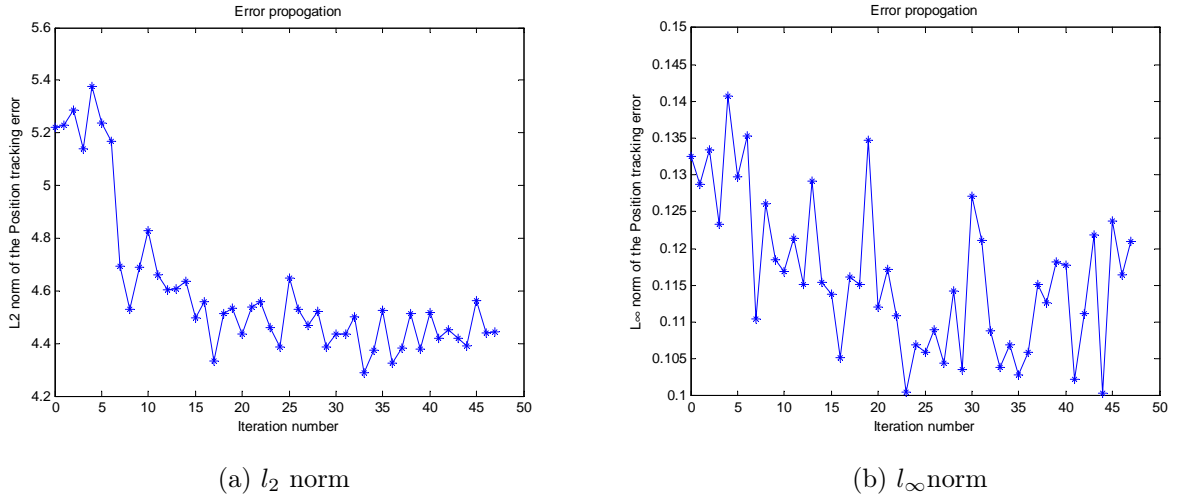


Figure 5.1: Norms of the simulated errors: ILC control law updated 7 times in 56 repetitions.

To further investigate the ILC stochastic performance. We simulate the system *with only the non-repetitive disturbances*, i.e., we set $\nu = 0$ in Fig. 4.6. Figure 5.2 shows the tracking error. It has an infinity norm of 0.1245 and a 2 norm of 4.1814.

Comparing this result with the one we obtained using the multi-iteration averaging method, we see that after about six updates of learning control, the error has reduced to about the same as the case without repetitive disturbance, indicating that the learning is successful.

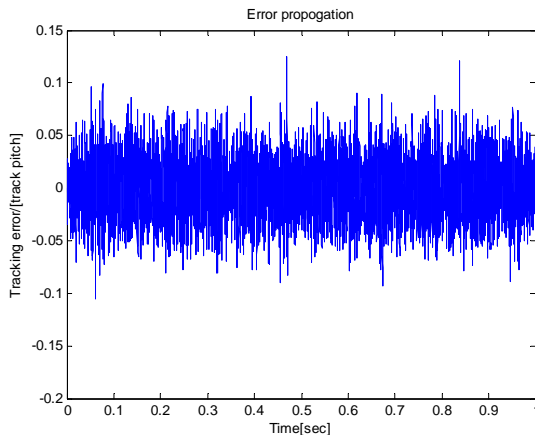


Figure 5.2: Simulated tracking errors when no external repetitive disturbance is present.

5.2 ILC Based on Adaptive Repetitive Error Estimation

Recall that our ILC control law is given by

$$u_{j+1}(k) = u_j(k) + Q_{ILC} (z^{-1}) L(z^{-1})e_j(k). \quad (5.3)$$

As has been mentioned in the last section, the key to reduce the influence of non-repetitive disturbance is to perform some averaging (or more generally, filtering) on $e_j(k)$. In this section, efforts are made to mathematically derive the optimal estimate of the *repetitive* components in $e_j(k)$, denoted as $\varepsilon(k)$, and then apply this estimate to the learning control law as shown in Fig. 5.3.

Definition 5.1. The repetitive error $\varepsilon(k)$ is defined as the tracking error when the system is subjected only to the repetitive output disturbance ν . The sources of $\varepsilon(k)$ include: plant modeling error and any repetitive disturbance.

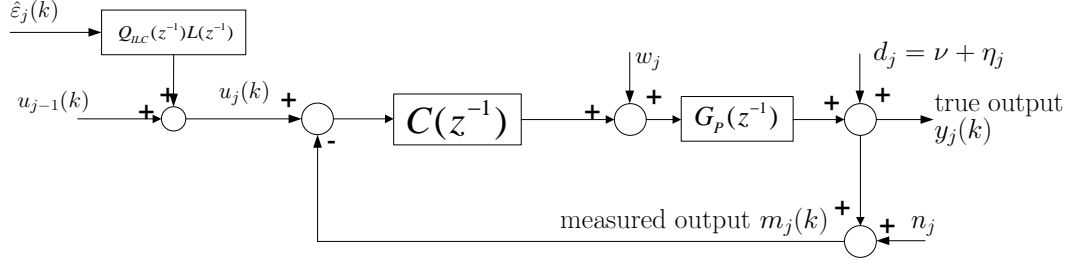


Figure 5.3: Block diagram of ILC based on adaptive repetitive error estimation

In Fig. 5.3, the measured error is given by

$$\begin{aligned}
 e_j(k) &= y_d(k) - m_j(k) \\
 &= y_d(k) - T_u u_j(k) - T_w w_j(k) - T_d(\nu(k) + \eta_j(k)) - T_n n_j(k) - n_j(k) \\
 &= \underbrace{(r(k) - T_u u_j(k) - T_d \nu(k))}_{\text{repeatable error } \varepsilon_j} - \underbrace{(T_w w_j(k) + T_d \eta_j(k) + T_d n_j(k) + n_j(k))}_{\text{nonrepeatable error } \bar{n}_j}
 \end{aligned}$$

where $\bar{n}_j(k)$ denotes the error caused by the non-repetitive disturbances w_j , η_j , and n_j .

To extract ε_j from e_j , we apply the least mean square error estimation to minimize the following cost function:

$$J_{j,k} = E [(\varepsilon_j(k) - \hat{\varepsilon}_j(k))^2], \quad (5.4)$$

which achieves its minimum at

$$\hat{\varepsilon}_j(k) = E[\varepsilon_j(k)] = E[e_j(k) + \bar{n}_j] = E[e_j(k)]. \quad (5.5)$$

The expectation can only be approximated from the empirical mean. We thus get the realizable best estimation of the repeatable error

$$\hat{\varepsilon}_j(k) = \frac{1}{j} \sum_{i=1}^{j-1} e_i(k) \quad (5.6)$$

Since the estimation is simply an averaging process, it is stable. The ILC update law is then modified to be

$$u_{j+1}(k) = u_j(k) + Q_{ILC}(z^{-1})L(z^{-1})\hat{\varepsilon}_{j+1}(k) \quad (5.7)$$

We now implement the above algorithm in the spiral servo writing project. Similar to Section 5.1, 56 spirals were written in simulation. The results are shown in Fig. 5.4. It is observed that after a transient response in the first two trials, the norms of the errors follow a decreasing trend. The l_2 and l_∞ norms decrease respectively to about 4.4 and 0.12 at the end of iteration 56, which are all close to the results without external repetitive disturbance (4.1814 and 0.1245). This indicates that we have effectively attenuated the repeatable error $\varepsilon(k)$ using the ILC algorithm.

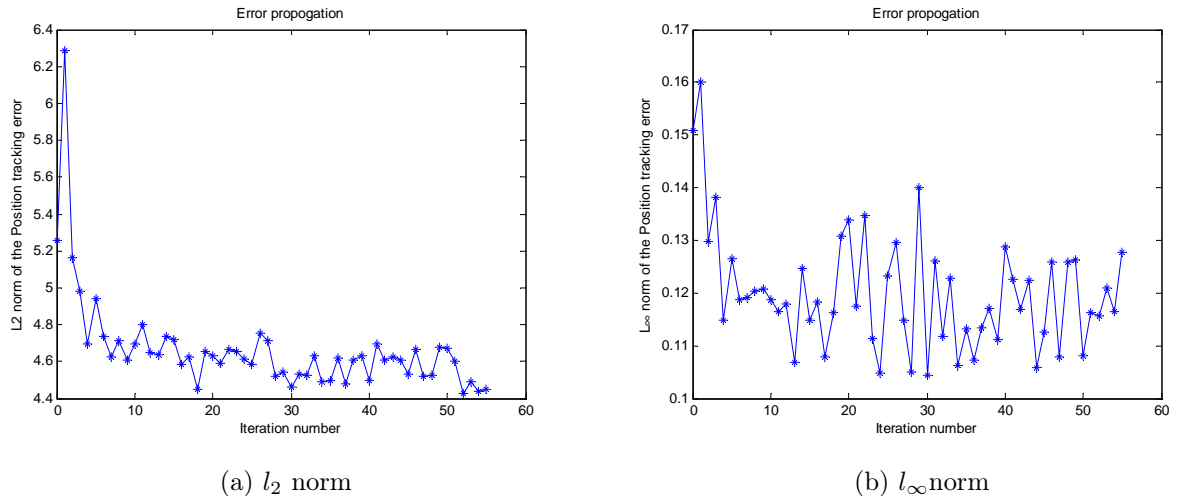


Figure 5.4: Norms of simulated errors: ILC based on adaptive minimum mean square repetitive error estimation.

5.3 ILC Based on Repeatable Disturbance Estimation

Section 5.2 investigated the estimation of repetitive error in ILC, which includes both the repetitive disturbance and the modeling error. When a good model is provided, it may be beneficial to directly compensate the repetitive disturbance. In this section, an repetitive disturbance rejection method is discussed. Figure 5.5 shows the configuration of the proposed algorithm.

where the second equality is derived using the fact that $P(z^{-1})w_j(k) - \eta_j(k) - n_j(k)$ is zero mean.

Notice that Eq. (5.8) can be transformed to

$$m_j(k) = \frac{PC}{1+PC} \left(u_j(k) + \frac{1}{PC} \nu(k) \right) + \left[\frac{P}{1+PC} w_j(k) + \frac{1}{1+PC} \eta_j(k) + \frac{1}{1+PC} n_j(k) \right] \quad (5.15)$$

The second part in the above equation is the contribution of the non-repetitive disturbances. To attenuate $\nu(k)$, the control law should be given by

$$u_j(k) = u_1(k) - \frac{1}{P(z^{-1})C(z^{-1})} \hat{\nu}_j(k) \quad (5.16)$$

The above control law requires a stable inverse of $P(z^{-1})C(z^{-1})$. As has been discussed before, ZPET algorithm can be used. To increase the system robustness, a (zero-phase) low-pass filter $Q(z^{-1})$ can be placed ahead of $\hat{\nu}_j(k)$, yielding

$$u_j(k) = u_1(k) - \frac{Q(z^{-1})}{P(z^{-1})C(z^{-1})} \hat{\nu}_j(k) \quad (5.17)$$

Simulating the algorithm in this section yields the results shown in Fig. 5.6. The ILC system response follow a similar decreasing pattern as the previous two cases in this chapter. The l_2 and l_∞ norms of the tracking error decrease respectively to about 4.6 and 0.12 at the end of iteration 56. The performance is slightly worse than the other two cases, due to the fact that only the output repetitive disturbance was attenuated.

To test the efficiency of the estimation, another simulation was conducted, where only the repetitive output disturbance ν was added to the system. A low pass filter $Q(z^{-1})$ with a cutoff frequency of 1000 Hz was applied. Figure 5.7b shows ν and $\hat{\nu}$ using the proposed estimation algorithm. It is observed that the low frequency part of the true disturbance was well estimated. From Fig. 5.7a, we see that the l_2 norm of the resulting tracking error decreased to its steady state value after two iterations, indicating a fast response of the ILC system.

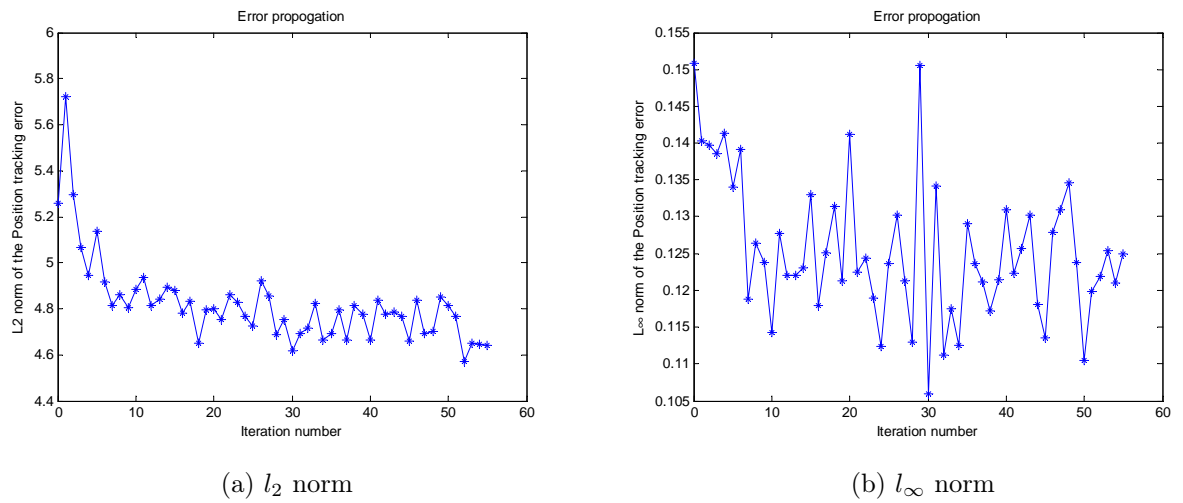


Figure 5.6: Norms of simulated errors: ILC based on non-repetitive disturbance estimation.

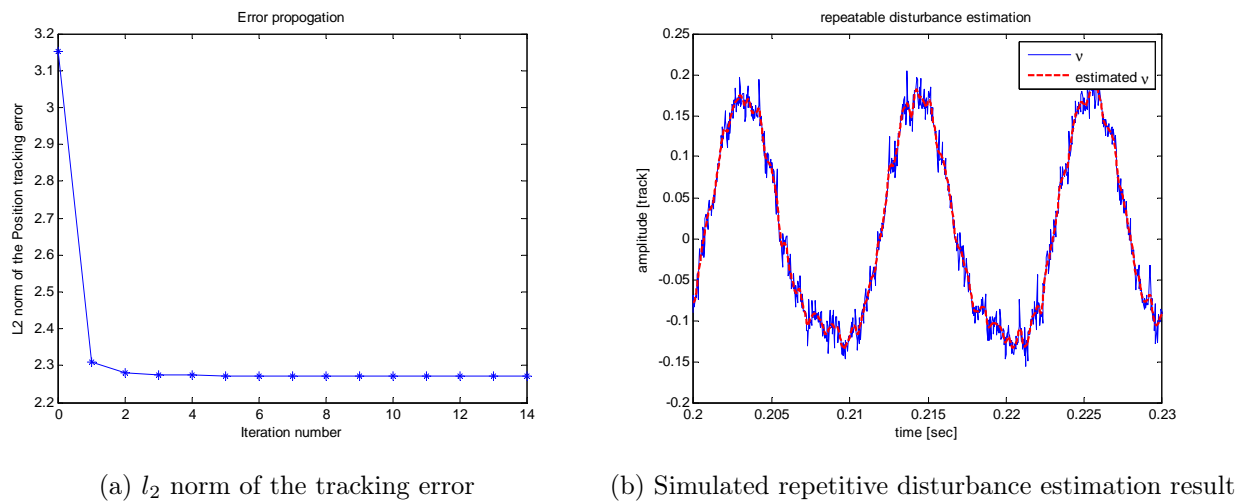


Figure 5.7: Repetitive disturbance rejection performance.

5.4 Summary

In this chapter, we have analyzed three different ILC algorithms to attenuate the influence of non-repetitive disturbances. All of the three are proved to be effective by

simulation. Yet, each algorithm has its own shortcoming. The multi-iteration ILC provides the deep error reduction but requires trials of system running without updating the control law. The adaptive repetitive error estimation method has relatively worse transient response. The repetitive disturbance estimation method only attenuates the influence of repetitive disturbances, ignoring the modeling errors. Choosing from the three should be based on the actual requirement and hardware restrictions.

Chapter 6

Conclusions and Future Research

In this report, the position control problem in spiral servo writing has been discussed. Two main control algorithms have been presented: the first applies ZPET, an optimal DOB to the position control of one stroke spiral writing; the second further introduces ILC with a ZPET learning filter to deal with the repetitive writing of multiple spirals. The controllers were evaluated on a benchmark problem. The controller performance was verified in both deterministic and noisy environments. The simulation results agree with the predicted system behavior.

Future research can be conducted on improving the stochastic ILC behavior in Chapter 5. The methods we presented all share the same central idea that they use the information from the previous iterations to improve the system performance in the future. This is essentially conducting signal processing/filtering in the iteration domain. Depending on how we set up the cost functions, various enhancement may be achieved.

Compensation of thermal induced disk deformation is another topic worth investigating. The rotating spindle motor on a servo track writer generates a great amount of heat which in turn results in thermal expansion to the disks mounted on the spindle. The distance between ID and OD of the disk could be increased by an order of about 40 tracks [16]. One possible way to address this problem would be to adjust the spiral writing velocity profile at the beginning of each trial. A scaling factor to the head velocity profile may be applied, based on the distance between the inner and

outer circular seed tracks measured during writing of the last spiral pattern.

Bibliography

- [1] A. Al Mamun, G. Guo, and C. Bi, *Hard disk drive: mechatronics and control*. CRC Press, 2007.
- [2] LaserResearch, “Mdeia servowriter,” <http://www.laserresearch.com>, December 2008.
- [3] M. Hirata, “Nss benchmark problem of hard disk drive system,” <http://mizugaki.iis.u-tokyo.ac.jp/nss/>.
- [4] Y. Mizoshita, S. Hasegawa, and K. Takaishi, “Vibration minimized access control for disk drives,” *IEEE Transactions on Magnetics*, vol. 32, no. 3 Part 2, pp. 1793–1798, 1996.
- [5] M. Tomizuka, “Zero phase error tracking algorithm for digital control,” *Journal of Dynamic Systems, Measurement, and Control*, vol. 109, no. 1, pp. 65–68, 1987.
- [6] C. Kempf and S. Kobayashi, “Discrete-time disturbance observer design for systems with time delay,” in *Proc. 1996 4th International Workshop on Advanced Motion Control*, vol. 1, Mar 1996, pp. 332–337 vol.1.
- [7] T. Murakami and K. Ohnishi, “Advanced motion control in mechatronics-a tutorial,” in *Proc. IEEE Workshop on Intelligent Motion Control*, vol. 1, 1990, pp. 9–17.
- [8] C. Kempf and S. Kobayashi, “Disturbance observer and feedforward design for a high-speeddirect-drive positioning table,” *IEEE Transactions on Control Systems Technology*, vol. 7, no. 5, pp. 513–526, 1999.

- [9] M. Tomizuka, “Zero phase error tracking algorithm for digital control,” *Journal of Dynamic Systems, Measurement, and Control*, vol. 109, no. 1, pp. 65–68, 1987.
- [10] T. Murakami and K. Ohnishi, “Advanced motion control in mechatronics-a tutorial,” in *Proc. IEEE Workshop on Intelligent Motion Control*, vol. 1, 1990, pp. 9–17.
- [11] X. Chen and M. Tomizuka, “Optimal plant shaping for high bandwidth disturbance rejection in discrete disturbance observers,” in *American Control Conference*, 2010.
- [12] B. Haack and M. Tomizuka, “The effect of adding zeroes to feedforward controllers,” *Journal of Dynamic Systems, Measurement, and Control*, vol. 113, p. 6, 1991.
- [13] M. Yamada, Y. Funahashi, and S. Fujiwara, “Zero phase error tracking system with arbitrarily specified gain characteristics,” *Journal of Dynamic Systems, Measurement, and Control*, vol. 119, p. 260, 1997.
- [14] S. Gunnarsson and M. Norrlof, “On the disturbance properties of high order iterative learning control algorithms,” *Automatica*, vol. 42, no. 11, pp. 2031–2034, 2006.
- [15] M. Norrlof and S. Gunnarsson, “Disturbance rejection using an ilc algorithm with iteration varying filters,” *Asian Journal of Control*, vol. 6, pp. 432–438, 2004.
- [16] U.S. Patent 7 193 797, 2007.

Appendix A

Proof of Theorem 4.1

Theorem 4.1 states that: In the proposed ILC control structure, the error caused by the repetitive disturbance ν can be perfectly attenuated, and the true error is updated by

$$e_{j+1}^o = (1 - T_u Q_{ILC} L) e_j^o + T_w (w_j - w_{j+1}) + T_d (\eta_j - \eta_{j+1}) + T_n (n_j - n_{j+1}) - T_u Q_{ILC} L n_j \quad (.1)$$

Proof. From the definition of the tracking error, e_{j+1}^o in Fig. 4.6 is given by

$$\begin{aligned} e_{j+1}^o &= y_d - y_{j+1} \\ &\Downarrow \text{substitute in Eq. (4.2)} \\ &= y_d - [T_u u_{j+1} + T_w w_{j+1} + T_d (\nu + \eta_{j+1}) + T_n n_{j+1}] \\ &\Downarrow \text{substitute in the control law Eq. (4.5)} \\ &= y_d - T_u (u_j + Q_{ILC} L e_j) - [T_w w_{j+1} + T_d (\nu + \eta_{j+1}) + T_n n_{j+1}] \\ &= y_d - T_u u_j - (T_u Q_{ILC} L) e_j - (T_w w_{j+1} + T_d (\nu + \eta_{j+1}) + T_n n_{j+1}). \end{aligned} \quad (.2)$$

Notice that

$$y_j = T_u u_j + T_w w_j + T_d (\nu + \eta_j) + T_n n_j.$$

Solving for $T_u u_j$ from the above equation and substituting the result to Eq. (.2),

we have

$$e_{j+1}^o = y_d - y_j - (T_u Q_{ILC} L) e_j + T_w w_j + T_d (\nu + \eta_j) + T_n n_j - [T_w w_{j+1} + T_d (\nu + \eta_{j+1}) + T_n n_{j+1}]. \quad (.3)$$

Noticing that the first two terms on the right hand side of Eq. (.3) equals to e_j^o and that $e_j = e_j^o + n_j$, we get

$$e_{j+1}^o = (1 - T_u Q_{ILC} L) e_j^o + T_d (\nu - \nu) + T_w (w_j - w_{j+1}) + T_d (\eta_j - \eta_{j+1}) + T_n (n_j - n_{j+1}) - T_u Q_{ILC} L n_j,$$

which is essentially the error propagation law in Eq. (.1). Additionally, the second term on the right hand side of the above equation equals 0 regardless of T_d . We see the repetitive disturbance ν is indeed perfectly rejected. \square